

Dislocation correlations in GaN epitaxial films revealed by EBSD and XRD

Vladimir M. Kaganer*, Domenik Spallek, Philipp John, Oliver Brandt, Jonas Lähnemann

Paul-Drude-Institut für Festkörperelektronik, Hausvogteiplatz 5–7, 10117 Berlin, Germany

Abstract

Correlations between dislocations in crystals reduce the elastic energy via screening of the strain by the surrounding dislocations. We study the correlations of threading dislocations in GaN epitaxial films with dislocation densities of $5 \times 10^8 \text{ cm}^{-2}$ and $1.8 \times 10^{10} \text{ cm}^{-2}$ by X-ray diffraction (XRD) in reciprocal space and by high-resolution electron backscatter diffraction (EBSD) in real space, where the strain is derived from a cross-correlation analysis of the Kikuchi patterns. The measured XRD curves and EBSD strain and rotation maps are compared with Monte Carlo simulations within one and the same model for the dislocation distributions. The screening of the dislocation strains is provided by creating pairs of dislocations with opposite Burgers vectors, with the mean distance between dislocations in a pair equal to the screening distance. The pairs overlap and cannot be distinguished as separate dipoles. The EBSD-measured autocorrelation functions of the strain and rotation components follow the expected logarithmic law for distances smaller than the screening distances and become zero for larger distances, which is confirmed by the Monte Carlo simulations. Screening distances of $2 \text{ }\mu\text{m}$ and $0.3 \text{ }\mu\text{m}$ are obtained for the samples with low and high dislocation densities, respectively. The dislocation strain is thus screened by only 4 neighboring dislocations. High-resolution EBSD allows for a more precise determination of the screening distances than from fits of the XRD curves. In addition, an anisotropic resolution of the EBSD measurements is observed and quantified.

Keywords: X-ray diffraction, electron backscatter diffraction, dislocations, strain, GaN

1. Introduction

It is well established that the elastic energy of a single straight dislocation per unit length of the dislocation line $E \propto (\mu b^2/4\pi) \ln(R/r_c)$ diverges as the lateral crystal size R is increased to infinity. Here μ is the shear modulus, b is the length of the Burgers vector, and r_c is the dislocation core radius ($r_c \approx 2.6b$) [1]. Hence, the elastic energy density of a crystal containing a finite density of random *uncorrelated* dislocations tends to infinity with increasing crystal size. Wilkens proposed [2] that the dislocations in a crystal are correlated, thereby screening the long range strain field from each other. He proposed a model of a “restrictedly random dislocation distribution”, where the crystal is subdivided into cells, with each cell containing the same number of dislocations. The numbers of dislocations with opposite Burgers vectors in a cell are equal, so that the total Burgers vector of a cell is zero and the total strain from the dislocations in a cell decays with the distance faster than the strain of an individual dislocation (in Wilkens’ model, the strain is assumed to be restricted within the cell). Then, the cell size R replaces the crystal size in the expression above for the elastic energy, and the energy density becomes independent of the crystal size.

This model was proposed in the framework of X-ray diffraction (XRD) line profile analysis of polycrystals, since the same divergence affects the widths of the diffraction lines. The strain probability density distribution calculated for screw dislocations in the Wilkens model [3] is used in computer programs for XRD line profile analysis [4, 5]. The fits of the experimental curves involve two parameters of the dislocation distribution, the dislocation density ρ and the cell size R . Although the initial formulation of the model implies that the cell size R is large compared to the mean distance between dislocations $\rho^{-1/2}$ (so that the number of the dislocations in a cell is large), in many cases these distances are comparable. A Monte Carlo simulation of the XRD profiles literally implementing the Wilkens model leads to artifacts when a cell contains one or only a few dislocation pairs [6]. An alternative model of the dislocation strain screening is to consider random pairs of dislocations with opposite Burgers vectors, with R being the mean distance between dislocations in a pair [7]. When the mean separation in a pair R exceeds the mean distance between all dislocations $\rho^{-1/2}$, the pairs overlap and cannot be distinguished as individual dipoles.

In many XRD studies, the dislocation density ρ is of primary interest, while the screening distance R serves as an auxiliary fit parameter required for an accurate determination of the dislocation density. However, the elastic energy stored in a crystal with dislocations is also of interest and requires an accurate determination of R [8]. In the XRD studies, the diffracted intensity is collected from the whole sample and the screening distance R is accessed only as a transition from a Gaussian shaped central part of the diffraction line to its $\propto q^{-3}$ tails. Recently, the scanning XRD microscopy technique has been developed to obtain

*Corresponding author.

Email address: kaganer@pdi-berlin.de (Vladimir M. Kaganer)

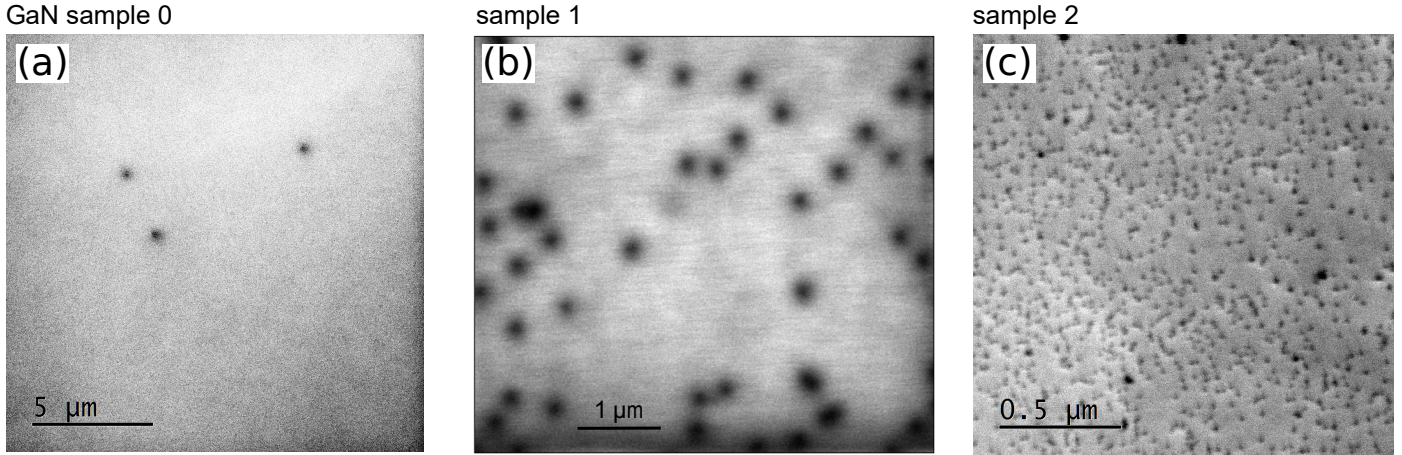


Figure 1: (a,b) Panchromatic cathodoluminescence intensity maps of GaN samples 0 and 1 and (c) scanning electron micrograph of sample 2.

maps of spatial distributions of strain and rotation tensors [9]. Such a study can be performed on a synchrotron and provides the strain averaged over the film thickness, due to the large penetration depth of the X-rays. This averaging does not affect the maps for the case of threading dislocations in (In,Ga)N films studied in Ref. [9], but for complicated three-dimensional dislocation distributions it may blur the maps up to a complete loss of information.

High-resolution electron backscatter diffraction (EBSD) provides maps of spatial distributions of the strain and rotation tensor components near the crystal surface obtained from shifts of the Kikuchi bands [10–12]. The strain sensitivity of the method reached 10^{-4} with the invention of the a cross-correlation based analysis of EBSD patterns [13, 14]. The strain and rotation maps and the strain probability density distributions have been reported in several studies [15–17]. The maps obtained in the present study are similar to those reported in the previous studies. However, the primary aim of our work is to obtain and analyze the spatial correlations of the strains, which was not addressed in these previous studies. We show that the strain-strain correlations calculated from the maps clearly reveal the dislocation strain screening by surrounding dislocations and provide the screening distances R .

The analysis of dislocations in GaN and other group III nitrides is of primary interest for optoelectronic applications of these materials and, at the same time, can serve as a touchstone for various methods of evaluating dislocation arrays. GaN epitaxial films contain threading dislocations oriented parallel to each other and perpendicular to the film surface. Such well-defined dislocation arrays allow a detailed modeling of both XRD curves and EBSD maps and their quantitative comparison. A respective comparison of different methods for dislocation density determination in metals [18] is much more complicated since it requires an account of several slip systems, grain boundaries, etc.

We study GaN(0001) epitaxial films with dislocation densities differing by orders of magnitude. We compare a film grown by metal-organic chemical vapor deposition with a threading dislocation density of $5 \times 10^8 \text{ cm}^{-2}$ and a film grown by molec-

ular beam epitaxy with a dislocation density of $1.8 \times 10^{10} \text{ cm}^{-2}$. A free standing GaN film with a dislocation density as low as $6 \times 10^5 \text{ cm}^{-2}$ and a perfect Si crystal are used as references.

We carry out both XRD and EBSD measurements on the same samples and also perform Monte Carlo simulations of the XRD line profiles and EBSD strain maps, using one and the same model of dislocation distributions for both experimental techniques and the same computing program. A comparison of the measured and Monte-Carlo-modeled strain maps in EBSD provides us with two further findings in addition to the determination of the screening distance for the dislocation strain. First, we find that the resolution of EBSD is highly anisotropic, with significantly worse resolution in the direction of the inclination of the incident electron beam. A quantitative estimate of the resolution is obtained by comparing the strain-strain correlations in two orthogonal directions. Secondly, we find that EBSD underestimates the strain for large dislocation densities in the sample grown by molecular beam epitaxy. This finding is considered to be the result of the dynamical diffraction of electrons in a crystal exhibiting a large strain gradient in the region where the diffracted beam is formed.

2. Experiment and Monte Carlo simulations

2.1. Samples

We study three GaN(0001) samples with different densities of threading dislocations (see Fig. 1). In all samples, the dislocations are straight lines running from the substrate to the film surface, along the surface normal. Hence, threading dislocations provide well defined arrays in single crystal samples suitable for both XRD and EBSD studies. The investigated samples were characterized in our previous works [19–21].

As a reference, we use a 350 μm -thick free-standing GaN (0001) film grown by hydride vapor phase epitaxy. We refer to it as sample 0. The dislocation density in this film is estimated from cathodoluminescence images to be as low as $6 \times 10^5 \text{ cm}^{-2}$. Since this sample produced an unexpectedly broad strain distribution in the EBSD measurements described in Sec. 3.2 below,

it was rinsed with isopropanol and ethanol and then cleaned with oxygen plasma to remove any contaminants and produce a uniformly oxidized surface layer. Etching of the surface with heated KOH removed this oxidized layer and left a smooth surface with a root-mean-square roughness of 0.31 nm. However, this cleaning step had very little effect on the EBSD maps.

Sample 1 is a 5.6- μm -thick GaN(0001) film on an Al_2O_3 (0001) substrate. A 1.3- μm -thick GaN layer is fabricated by plasma-assisted molecular beam epitaxy on top of a 4.3- μm thick GaN(0001) template, which in turn is grown by metal-organic chemical vapor deposition on an Al_2O_3 (0001) substrate. As this sample has been grown for our former study [20, 21], an additional 3-nm-thick (In,Ga)N single quantum well is buried at about 650 nm below the surface, which however is not relevant for the present work. Threading dislocations, which are in the focus of the present study, are inherited from the template. Figure 1(b) presents a cathodoluminescence (CL) intensity image of this sample. Dislocations are seen as dark spots since they act as centers of nonradiative recombination of excitons [22–26]. The density of the spots is $5 \times 10^8 \text{ cm}^{-2}$. We note that the counting of the dark spots on CL images may underestimate the density of threading dislocations [27].

Sample 2 has been grown for another study of ours [19]. A 2.5- μm -thick GaN(0001) film is grown by plasma-assisted molecular beam epitaxy on a 6H-SiC(0001) substrate. A cathodoluminescence image of this sample shows overlapping dark spots because of the large dislocation density, which does not allow an accurate determination of the dislocation density. Figure 1(c) presents a scanning electron micrograph of this sample. It shows dark spots with the density of $1.8 \times 10^{10} \text{ cm}^{-2}$. These spots have been identified as pits at dislocation outcrops by comparing a similar electron micrograph of sample 1 with the CL map taken from the same surface area [21]. For the sample with a low dislocation density, a one-to-one correspondence of the pits with the dark spots in the CL image has been observed.

Additionally, a reference EBSD measurement is obtained on a Si(001) wafer.

2.2. X-ray diffraction

The XRD measurements were carried out with $\text{CuK}\alpha_1$ radiation using a Panalytical X’Pert diffractometer equipped with a two-bounce Ge(220) hybrid monochromator. The measurements were performed using the skew diffraction geometry [28–30] in a double-crystal setup.

2.3. Electron backscatter diffraction

Scanning electron microscopy (SEM) and CL imaging, as well as the EBSD measurements were carried out in a Zeiss Ultra 55 scanning electron microscope. For the EBSD measurements, the microscope was operated at an acceleration voltage of 15 kV with a beam current of 6 nA. To record the Kikuchi patterns, the stage with the mounted sample was tilted by 70° with respect to the incident beam direction towards an EDAX Hikari Super EBSD detector.

The patterns were recorded with the highest available resolution of 470×470 pixels and background-corrected using a reference pattern. EBSD maps were recorded over either $2 \times 2 \mu\text{m}^2$

or $10 \times 10 \mu\text{m}^2$ areas with step sizes of 20 nm and 50 nm, respectively, at an exposure time of 100 ms. Measurements with these settings took approximately 20 min for the smaller maps and 80 min for the bigger maps to record. Sample drift was estimated by comparing SEM images recorded before and after the measurement and were smaller than 18% of the map dimensions, indicating negligible drifts per recorded pixel but a potential warping of the spatial resolution.

The cross-correlation analysis of the Kikuchi patterns¹ [32] was carried out with the software CrossCourt 4.5.3.6 by BLG Vantage. Examples of Kikuchi patterns from all four samples are presented in Fig. S1 in the Supplementary Material (SM). 20 regions of interest on the Kikuchi patterns were referenced for the calculations of the cross-correlation function. From these calculations, maps of the strain and rotation tensor components with a sub-pixel resolution were obtained using the elastic moduli of GaN [33]. A remapping of the resulting maps had a minor influence on the strain distribution and was not applied for the shown data.

2.4. Monte Carlo simulations

Monte Carlo simulations of both XRD curves and EBSD maps are performed in the framework of one and the same model of dislocation arrangements and dislocation strains using the computing programs that were developed earlier for XRD [19, 34] and adapted here for EBSD. The displacement fields of a -type edge dislocations with Burgers vectors $1/3 \langle 11\bar{2}0 \rangle$, c -type screw dislocations with Burgers vectors $\langle 0001 \rangle$, and $a+c$ -type mixed dislocations with Burgers vectors $1/3 \langle 11\bar{2}3 \rangle$ are calculated. The screening of the dislocation strains by surrounding dislocations is provided by generating dislocations in pairs with opposite Burgers vectors. The positions of the pairs are random and uncorrelated. The distances between dislocations in the pairs are assumed to follow a lognormal distribution with a mean value of R (hereafter referred to as the screening distance) and a standard deviation of $R/2$. The XRD intensity $I(q)$ is calculated as a probability density of the distortion component $q = \hat{\mathbf{K}}^{\text{out}} \cdot \nabla(\mathbf{Q} \cdot \mathbf{U})$, where $\mathbf{U}(\mathbf{r})$ is the total displacement due to all dislocations, \mathbf{Q} is the diffraction vector, and $\hat{\mathbf{K}}^{\text{out}}$ is the unit vector in the direction of the diffracted beam [19, 34]. It is worth noting that the direction $\hat{\mathbf{K}}^{\text{out}}$ emerges in the diffraction from a single crystal as a consequence of the intensity integration performed by a widely open detector over the plane in reciprocal space perpendicular to \mathbf{K}^{out} . In powder diffraction, the respective intensity integration from randomly oriented grains is performed over the plane perpendicular to the diffraction vector. In this case, $\hat{\mathbf{K}}^{\text{out}}$ is replaced with the unit vector in the direction of \mathbf{Q} [30]. The EBSD maps are simulated by calculating all components of the strain tensor $\varepsilon_{ij} = (\partial U_i / \partial x_j + \partial U_j / \partial x_i) / 2$ and the rotation tensor $\omega_{ij} = (\partial U_i / \partial x_j - \partial U_j / \partial x_i) / 2$, using the same displacement vector $\mathbf{U}(\mathbf{r})$. For the XRD simulations, it is sufficient to use the displacement field of a straight dislocation

¹Early studies distinguish Kikuchi patterns formed by electron diffraction in transmission electron microscopy, and pseudo-Kikuchi patterns due to diffraction of backscattered electrons in SEM [31]. Nowadays, the term Kikuchi pattern is used for both of them.

in an infinite crystal, as the X-ray intensity is collected over the entire film thickness. The displacement for a dislocation along the $\langle 0001 \rangle$ direction in a hexagonal crystal is employed. It coincides with the isotropic solution with the Poisson ratio taken to be $\nu_h = c_{12}/(c_{11} + c_{12})$ ([35], Sec. 2.5). Here c_{ij} are the elastic moduli. Using their values for GaN [33], we obtain $\nu_h = 0.27$. For the EBSD simulations, the elastic strain relaxation at the free surface is taken into account. We have compared the isotropic solution ([36], Sec. 6.3) with a more comprehensive anisotropic solution for a dislocation along the sixfold axis ([35], Sec. 2.5). The difference is negligible compared to the statistical errors in the Monte Carlo simulations presented below.

3. Results

3.1. X-ray diffraction

Figures 2(a) and 2(b) show by thick gray lines measured XRD curves for several reflections from samples 1 and 2, respectively. A symmetric Bragg reflection 0002 and two asymmetric ones,² 11 $\bar{2}$ 4 and 2 $\bar{2}$ 02, are presented. Some qualitative conclusions can be drawn from a direct comparison of the curves. The diffraction vector of the symmetric reflection is directed along the lines of threading dislocations. Consequently, this reflection is only sensitive to screw dislocations and screw components of mixed dislocations, which produce displacements in the direction of the dislocation lines. The widths of the symmetric and asymmetric reflections from sample 1 are closely comparable, indicating similar densities of screw and edge dislocations. In contrast, the symmetric reflection from sample 2 is notably narrower than the asymmetric reflections from this sample, which is due to a low density of screw dislocations in comparison with the edge ones. Comparing diffraction curves from the two samples, one can see that the density of screw dislocations in sample 2 is smaller than in sample 1, while the density of edge dislocations is notably larger.

The thin black lines in Figs. 2(a,b) represent Monte Carlo simulations of the respective diffraction curves. As screw dislocations are very uncommon in GaN films grown by metal-organic chemical vapor deposition, we have assumed a density of $8 \times 10^8 \text{ cm}^{-2}$ of mixed $a+c$ -type dislocations for sample 1. The screening distance is taken to be $R = 1 \mu\text{m}$. For sample 2, grown by molecular beam epitaxy, edge dislocations of a density of $5 \times 10^{10} \text{ cm}^{-2}$ with the screening distance $R = 0.3 \mu\text{m}$ are taken to simulate the asymmetric reflections. The symmetric Bragg reflections are simulated by screw dislocations with a density of $5 \times 10^8 \text{ cm}^{-2}$, which is two orders of magnitude smaller than the density of edge dislocations. Their screening distance is taken as $R = 0.7 \mu\text{m}$. The contribution of screw dislocations to the asymmetric XRD profiles of sample 2 is negligible and they are not considered in the further analysis.

²We refer to these reflections as asymmetric following the common tradition. In fact, the diffraction vectors of these reflections are inclined with respect to the surface normal, and these reflections are asymmetric in coplanar diffraction. In skew geometry, however, these reflections are symmetric (the incident and the diffracted waves make equal angles with the crystal surface) and non-coplanar (the scattering plane does not contain the surface normal) [30].

We fit both the measured and the Monte-Carlo-simulated XRD curves in the same way, following Ref. [30]. The symmetric reflections are fitted first to get the densities of screw dislocations, and their contributions are taken into account in the fits of the asymmetric reflections, which give the densities of the edge dislocations. Each reflection is fitted independently from the others. The two essential fitting parameters are the dislocation density ρ and the screening distance R . Figures 2(c,d) present by full symbols the values of ρ and R obtained in the fits of the measured XRD curves, while open symbols are the results of the corresponding fits of the Monte-Carlo-simulated curves. The data are plotted as a function of the angle Ψ between the diffraction vector and the surface. Thus, $\Psi = 0$ corresponds to an in-plane reflection and $\Psi = 90^\circ$ to a symmetric Bragg reflection. Plotting the fit parameters as a function of Ψ is just a convenient way of presenting the data: ideally, no variation of the parameters is expected. The fits of the measured and simulated XRD profiles in different reflections from both samples show a small scatter in the values of the dislocation density ρ and a notably larger scatter in the values of R . This behavior results from the fact that the fit formula [30] accurately accounts for the orientation prefactor (a ‘contrast factor’) for the dislocation density. However, calculation of a respective prefactor for R is considerably more difficult and has not been attempted here. Its absence does not affect the determination of the dislocation density, which was the primary aim of the fits, but introduces a scattering of the values of R . The EBSD study presented in the next section complements this reciprocal-space analysis by XRD with a real-space observation of the dislocation correlations, and allows for an accurate determination of the screening distance R . The values of R obtained from EBSD maps are marked in Fig. 2(d) by dashed lines for comparison.

3.2. Electron backscatter diffraction: experiment

Figures 3(a–c) present maps of the strain component ε_{22} of the GaN samples 0, 1, and 2 obtained from the analysis of the EBSD measurements. Complete sets of maps of the six components of the strain tensor ε_{ij} and the three components of the rotation tensor ω_{ij} are presented in the SM, Figs. S2, S3, and S4. As the EBSD maps are relative to an arbitrarily chosen reference value, we set the mean value of each map to zero. We follow the standard EBSD axes notation: the sample surface is the xy plane, the y axis is oriented such that the incident electron beam (inclined by 70° with respect to the surface normal) is in the yz plane. The sizes of the maps, $10 \times 10 \mu\text{m}^2$ for sample 1 and $2 \times 2 \mu\text{m}^2$ for sample 2, are chosen to cover a sufficiently large number of dislocations, of the order of 10^3 , for a statistical analysis.

In a $2 \times 2 \mu\text{m}^2$ map of sample 0, just a single dislocation can be expected with a probability of 25%, compared to some 10^3 dislocations in the maps of samples 1 and 2. So, sample 0 can be considered as dislocation free on the scale of the EBSD measurements. Nevertheless, the range of the strain variation in Fig. 3(a) is comparable with that in samples 1 and 2. In contrast to these latter samples, the strain map does not reveal correlations between strains in neighboring measurement points, which

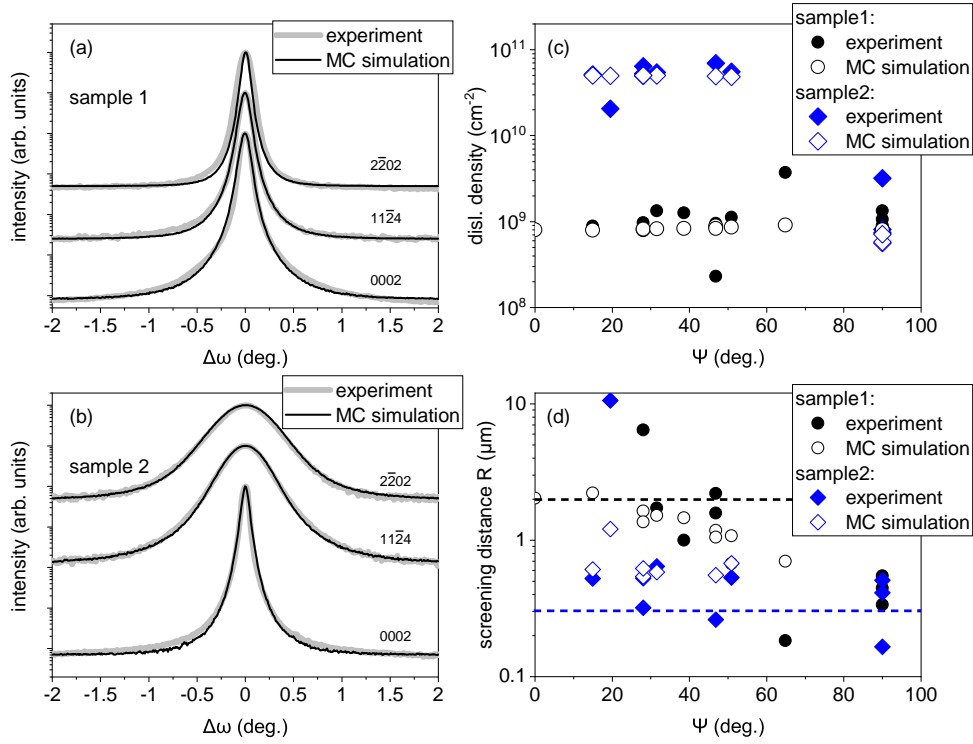


Figure 2: (a,b) X-ray diffraction curves of samples 1 and 2 (thick gray lines) and their Monte Carlo simulations (thin black lines). (c,d) Dislocation density and the screening distance R obtained in the fits of the experimental (full symbols) and the simulated (open symbols) curves. The fits for different reflections are made independently and presented as a function of the angle Ψ between diffraction vector and surface. The parameters for sample 1 are presented by black symbols, and for sample 2 by blue symbols. Dashed lines in (d) mark the values of screening distances obtained in the analysis of EBSD maps.

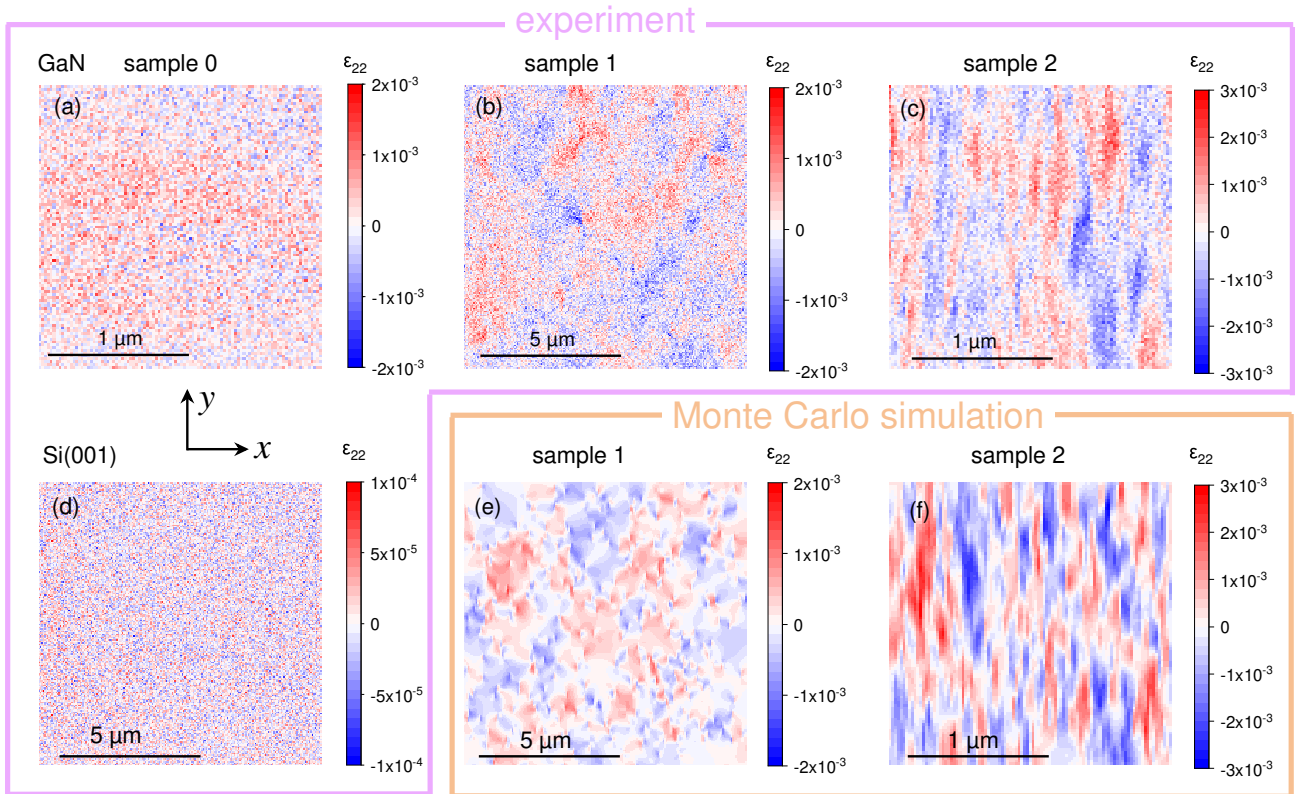


Figure 3: EBSD maps of the strain component ϵ_{22} (a–c) in GaN samples 0, 1, and 2 and (d) in a Si(001) wafer, and (e,f) Monte Carlo simulation of the ϵ_{22} maps for samples 1 and 2. Note that the strain obtained for Si(001) is an order of magnitude lower than in the GaN samples.

is quantified below by calculation of the strain–strain correlations. Since the strain range for sample 0 in Fig. 3(a) is an order of magnitude larger than the expected sensitivity of the EBSD measurements, the same measurement has been performed on a Si(001) wafer as presented in Fig. 3(d). The map also displays uncorrelated random noise, but the range of strain variations is of the order of 10^{-4} , which is the expected sensitivity of high-resolution EBSD [13, 14] and an order of magnitude smaller than in all GaN samples under investigation. A whole set of the maps of all components of the strain and rotation tensor are presented in Fig. S5 in the SM and show the variations in the same range of 10^{-4} .

The map of ε_{22} from sample 2 in Fig. 3(c) shows a notable difference between the x and y directions, with all features being extended in the y direction. Figure S4 shows a similar anisotropy in the maps of all strain and rotation components of this sample. We have performed the same measurement with the sample rotated by 90° around its normal and found that the direction of the extension in the maps is also rotated by 90° to the new y direction. A possible anisotropy of the sample is thus ruled out and it is established that the features in the maps are extended along the direction of the tilt of the incident electron beam. We show below that this extension is explained by a strongly anisotropic resolution of the EBSD measurements, and quantify this anisotropy.

Figure 4(a) presents by red and blue lines the probability distributions of the strain ε_{22} obtained from the maps of samples 1 and 2 in Figs. 3(b) and 3(c). The dashed orange line is a similar distribution obtained from the map of the dislocation free GaN sample 0 in Fig. 3(a), while the thin black line is the respective distribution from the Si(001) sample in Fig. 3(d). A comparison of the widths of the strain distributions from dislocation free GaN and Si samples points to a material specific broadening for GaN. The possible origin of this broadening is discussed in Sec. 4 below. The contribution of dislocations in samples 1 and 2 to the widths of the strain distributions is only moderate.

The shear strains ε_{13} and ε_{23} are of separate interest. Since the information depth of EBSD is small (less than 20 nm), the conditions of the stress-free surface $\sigma_{i3} = 0$ ($i = 1, 2, 3$), are satisfied. One of these conditions, $\sigma_{33} = 0$, is used in the processing of the Kikuchi patterns, since only the differences of the strains $\varepsilon_{11} - \varepsilon_{33}$ and $\varepsilon_{22} - \varepsilon_{33}$ can be found from the positions of the Kikuchi bands and this condition allows the three normal strain components to be determined separately [16]. The other two conditions $\sigma_{i3} = 0$ ($i = 1, 2$) are not used in the processing of the Kikuchi patterns. Since $\sigma_{i3} = 2c_{44}\varepsilon_{i3}$ ($i = 1, 2$) in a hexagonal crystal, the strains ε_{13} and ε_{23} must be zero at the free surface. Figure 4(b) shows the probability distributions of ε_{13} obtained from the respective EBSD maps of GaN samples 0, 1 and 2 as well as the silicon wafer. The probability distributions of the other shear strain component ε_{23} are about two times narrower than those of ε_{13} . The maps of these components (shown in Figs. S2–S5 of the SM) exhibit uncorrelated random noise, as do all maps of the GaN sample 0 and the Si wafer. Figure 4(b) shows that all three GaN samples possess the same width of the ε_{13} distribution, which is 16 times larger than the respective distribution for Si, and a factor of 2 narrower than

the distribution of ε_{22} from sample 0 in Fig. 4(a). Hence, the non-zero shear strains ε_{13} and ε_{23} are material specific. We postpone further discussion to Sec. 4.

Figures 5(a,b) and 6(a,b) present the strain-strain correlations calculated from the maps of ε_{22} in Figs. 3(a,b) and from similar maps of other strain components presented in Figs. S3 and S4. We calculate the correlation functions as averages $\langle \varepsilon(\mathbf{r}_1)\varepsilon(\mathbf{r}_2) \rangle$ over the respective maps. Figure 5 shows correlations in x and y directions (the difference $\mathbf{r}_1 - \mathbf{r}_2$ is directed either along x or y), while Fig. 6 shows correlations as a function of the distance $r = |\mathbf{r}_1 - \mathbf{r}_2|$ averaged over all orientations of $\mathbf{r}_1 - \mathbf{r}_2$. Since the strain of a single dislocation decays with the distance as $\varepsilon(r) \propto r^{-1}$, we expect the correlations to decay as $\ln |\mathbf{r}_1 - \mathbf{r}_2|$ as long as $|\mathbf{r}_1 - \mathbf{r}_2|$ is less than the distance R , at which the dislocation strain is screened by surrounding dislocations, and to become zero at larger distances. We therefore plot the correlations in Figs. 5 and 6 as a function of the logarithm of the distance. The expected linear decay of the correlations in this scale and a kink from the logarithmic decay to zero correlations are clearly seen in Figs. 6(a,b) and allow the determination of the screening distances: these distances are 2 μm for sample 1 and 0.3 μm for sample 2. This finding is the main result of the present paper.

Figures 6(a,b) also show a drastic difference in the correlations between the in-plane strain components ε_{11} , ε_{12} , ε_{22} and the shear strains ε_{13} , ε_{23} . The latter ones are expected to be zero due to zero stress conditions at the free surface but show distributions in Fig. 4(b) comparable in width to the in-plane strains. Their correlation functions in Figs. 6(a,b) are negligibly small compared to the correlations of the in-plane strains and quantify the visual impression of the respective maps in Figs. S3 and S4 as uncorrelated random noise.

One can see in Figs. 5 and 6 deviations from straight lines (i.e. from the logarithmic law) at separations smaller than about 200 nm: the curves are gradually flattened. One can also see in Fig. 5(b) a strong difference between correlations of ε_{11} and ε_{22} and a strong difference between the correlations of ε_{22} in x and y directions. This plot thus quantifies the anisotropy of the map of ε_{22} from sample 2 noted above. The respective plots for sample 1 in Fig. 5(a) do not show such a difference between correlations of ε_{11} and ε_{22} and between the x and y directions because of the larger step size employed for these maps.

3.3. Electron backscatter diffraction: Monte Carlo simulations

We simulate the maps of all strain and rotation components by the Monte Carlo method, as described in Sec. 2.4. We take the dislocation densities $5 \times 10^8 \text{ cm}^{-2}$ and $1.8 \times 10^{10} \text{ cm}^{-2}$ for samples 1 and 2, as determined in Sec. 2.1, and the mean distances between dislocations in the pairs of 2 μm and 0.3 μm , respectively, as derived above from the plots in Fig. 6(a,b). We simulate maps having the same areas and number of pixels as in the experiment, with the aim to obtain the same level of statistical errors due to averaging over the same number of dislocations. The strains are integrated over a 20 nm thick layer at the surface, corresponding to the information depth of EBSD measurements. The simulated maps of ε_{22} in Fig. 3(e,f), as well as the simulated maps of all strain and rotation components shown in Figs. S6

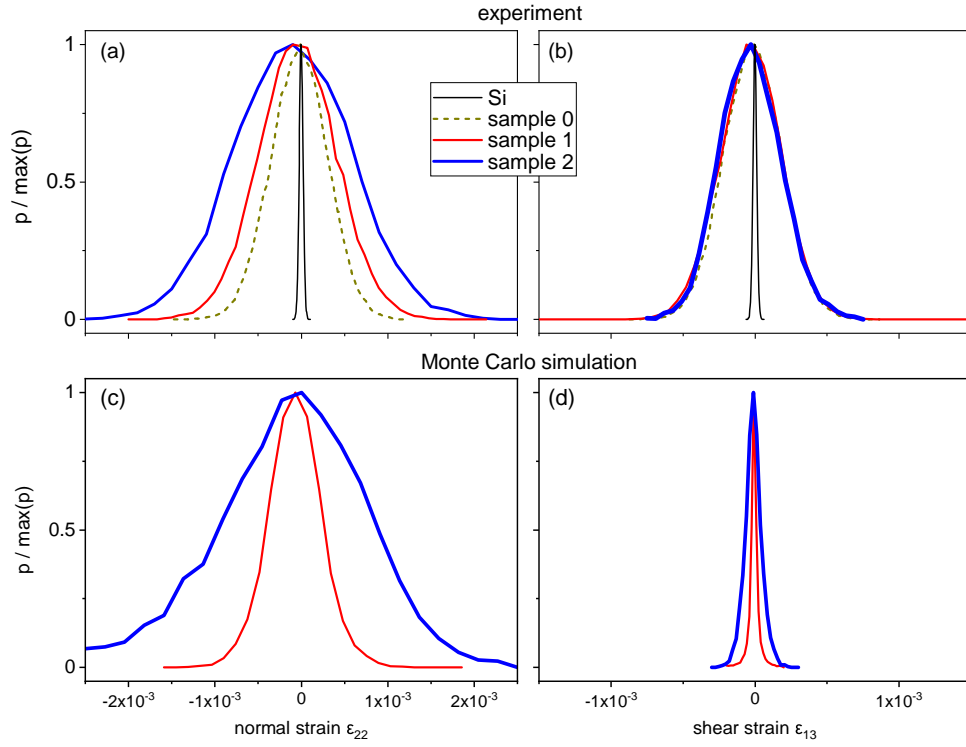


Figure 4: Top row: probabilities of (a) normal strain component ϵ_{22} and (b) shear strain component ϵ_{13} in samples 1 and 2, as well as in the reference dislocation free GaN sample (sample 0) and a silicon wafer, obtained from the maps in Figs. 3(a-d). Bottom row: probabilities of (c) normal strain component ϵ_{22} and (d) shear strain component ϵ_{13} in the Monte Carlo simulated maps in Figs. 3(e,f) and S3, S4. The probabilities are scaled by their maxima.

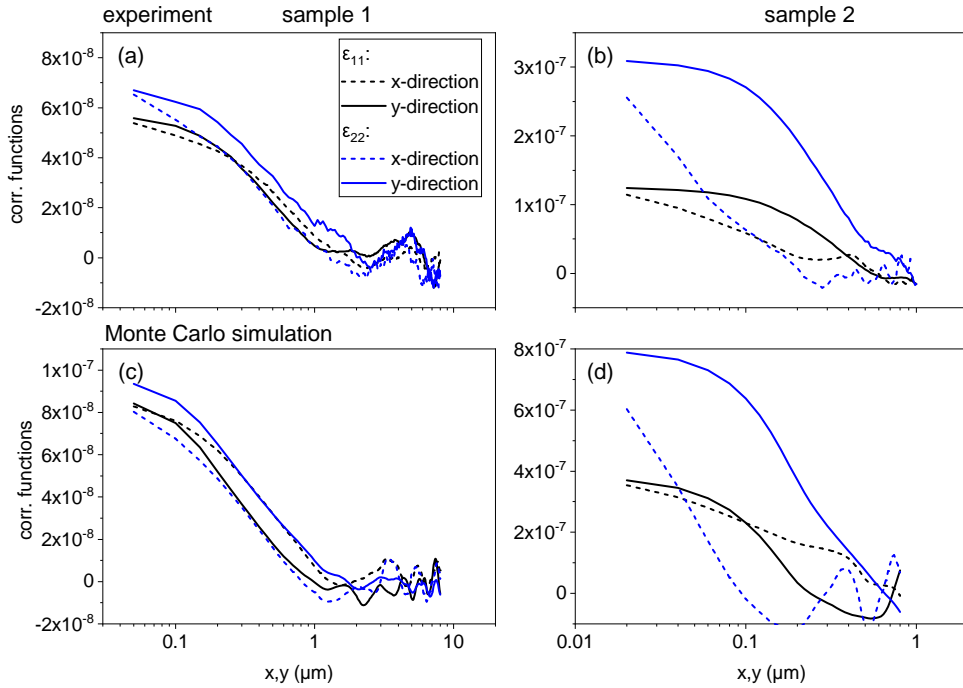


Figure 5: Strain-strain correlation functions of (a,b) samples 1 and 2 and (c,d) their Monte Carlo simulations.

and S7 show a good qualitative agreement with the measured maps.

To make a quantitative comparison, we process the simulated maps to obtain the correlation functions in the same way as done for the measured maps. An agreement between simulations and experiment for sample 2 is reached when we introduce a strongly anisotropic resolution to the simulated maps. Specifically, the calculated strains are averaged over an area $20 \times 200 \text{ nm}^2$, extended in the direction of inclination of the incident electron beam. Such a resolution allows to reach an agreement between the correlations in x and y directions, as seen in Figs. 5(b) and 5(d). The same resolution is imposed for sample 1 but does not give rise to a similar anisotropy of the maps, because the measurements are performed with a larger step size, to cover a larger surface area. As a result, both the experimental and the simulated correlation curves of sample 1 in Figs. 5(a) and 5(c) do not show the anisotropy observed for sample 2.

The measured strain distribution of sample 1 in Fig. 4(a) is slightly broader than the respective Monte Carlo simulation in Fig. 4(c). The additional broadening can be attributed to the apparent strain observed in sample 0 and discussed further in Sec. 4.4, which is independent of the dislocation strain.

Figure 4(d) presents the probability distributions of the strain component ε_{13} obtained from the Monte Carlo simulated maps of samples 1 and 2 in Figs. S6 and S7, respectively. This strain is equal to zero at the surface due to the strain-free boundary conditions, and the non-zero strains result from the integration of strains over the 20 nm-thick layer at the surface corresponding to the information depth of EBSD. The widths of the probability distributions of ε_{13} in the simulated maps in Fig. 4(d) are at least by a factor of 5 smaller than the respective experimental widths in Fig. 4(b). Hence, the strains ε_{13} , ε_{23} in the experimental maps are not the strains near the surface. They look, similarly to all maps of the dislocation-free sample 0, like uncorrelated random noise and may have the same origin, which is discussed in Sec. 4.4.

The orientation-averaged correlation curves in Fig. 6(c,d), obtained from the Monte Carlo simulated maps, reveal the logarithmic decay of the strain correlations (straight lines in the coordinates of the figure) and a kink as a transition to zero correlations at distances exceeding the screening distance. The positions of the kinks coincide with the screening distances of $2 \mu\text{m}$ and $0.3 \mu\text{m}$ for samples 1 and 2 respectively, taken as an input of the Monte Carlo simulations. A gradual increase of correlations is seen at distances smaller than the resolution of 200 nm. Similar correlation functions for the different rotation components, both measured and Monte-Carlo simulated, are shown in Fig. S8 in the SM. They reveal the same logarithmic decay of correlations at distances smaller than R and the absence of correlations at larger distances, where the characteristic kink is seen at the same distances R as in the strain correlations of the respective samples.

4. Discussion

4.1. Strain distributions in XRD and EBSD

Both XRD profiles and probability distributions obtained from EBSD maps represent distributions of strains and rotations, as it was already pointed out and compared by Wilkinson *et al.* [15]. Measurements by these two methods are complimentary. The XRD intensity provides the probability distribution over several orders of magnitude down from the maximum, allowing the dislocation density ϱ and the dislocation strain screening distance R to be determined from a single profile. However, the XRD intensity is an average over the sample volume and potentially includes a contribution from strained regions far from the surface, in particular the film–substrate interface. EBSD, in turn, provides the maps of strains and rotations at the surface. The statistics of the strain maps are limited by the number of pixels in the map. The maps can be used to determine not only the strain probability distributions, but also the spatial correlations of strains and rotations, which allows the screening distance R to be determined directly as the distance at which the correlations become zero. A comparison of the dislocation correlations obtained by the two methods is the main aim of the present paper.

We have compared in Fig. 2, the measured XRD curves, their Monte Carlo simulations, and fits of both sets of curves by the formula proposed in Ref. [30]. A comparison of a curve simulated by the Monte Carlo method with the fit of this curve provides a check on the internal consistency of simulations and fits: dislocation densities obtained from fits of simulated curves (open symbols in Fig. 2(c)) coincide with the input values of the simulations with fairly little scatter.

The dislocation densities that are obtained in the Monte Carlo simulations and confirmed by the fits of the XRD curves are larger than the spot densities obtained from Fig. 1 by factors of 1.6 and 2.7 for samples 1 and 2, respectively. It is noteworthy that our previous studies [30, 37] also yielded dislocation densities obtained from the XRD profiles that were several times larger than those determined by transmission electron microscopy. Since XRD collects intensity scattered from the whole volume of the GaN film, the additional broadening of XRD curves can be caused by strain originating from the film–substrate interface. However, calculations [37] show that misfit dislocations at the film–substrate interface modify the reciprocal space maps but, for thick films, have little effect on the double-crystal curves that are measured in the present work.

4.2. Screening distances

The screening of dislocation strains by surrounding dislocations provides a transition from the Gaussian central part of the XRD profile to the $I(q) \propto q^{-3}$ tails. The screening distance R is a second parameter, in addition to the dislocation density ϱ , that is included in the fit of the XRD profiles [30]. The screening distances obtained by fitting the experimental curves (full symbols in Fig. 2(d)) agree with those obtained from correlations in EBSD maps (horizontal dashed lines in Fig. 2(d)), although there is a rather large scatter between the values obtained from different reflections.

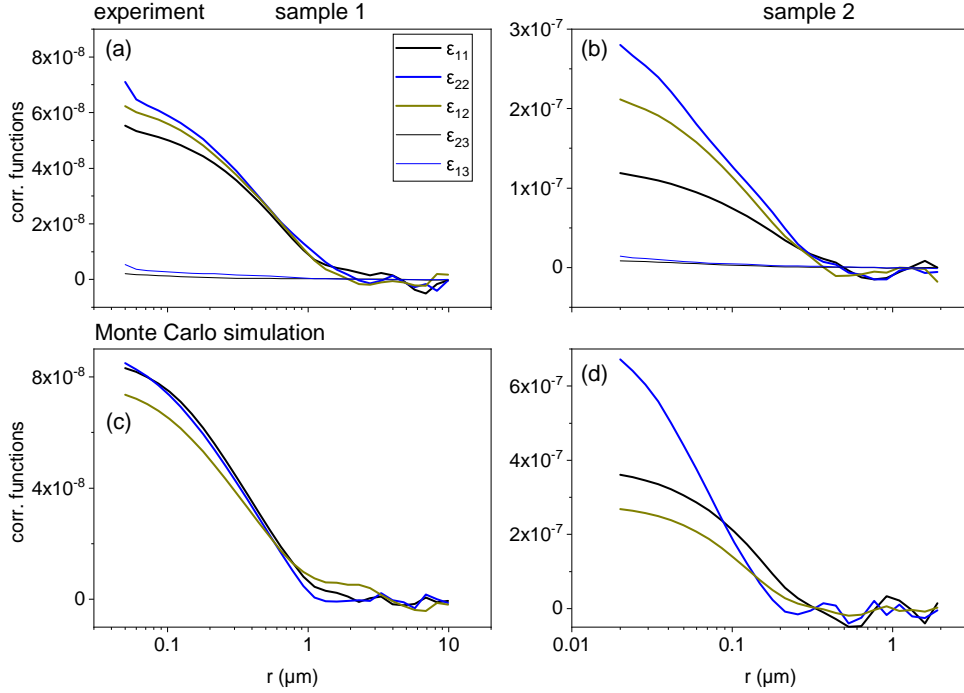


Figure 6: Orientation-averaged strain–strain correlation functions of (a,b) samples 1 and 2 and (c,d) their Monte Carlo simulations.

Plots of the autocorrelation functions of the components of the strain and rotation tensors measured by EBSD provide a more robust tool for determining the screening distance R . This distance is clearly seen as a kink in the plot of the correlation function in dependence of the logarithm of the separation, and is found to be the same for all strain and rotation components. We find screening distances R of $2 \mu\text{m}$ and $0.3 \mu\text{m}$ for the GaN films with threading dislocation densities ρ of $5 \times 10^8 \text{ cm}^{-2}$ and $1.8 \times 10^{10} \text{ cm}^{-2}$, respectively. In both cases, the number of dislocations that provide screening of the strain of a given dislocation $M = R\rho^{1/2}$ is about 4. This means that the dislocation strain field is very effectively screened by only a few surrounding dislocations. To obtain these screening distances, we measure the strain and rotation maps over areas with linear sizes that are large compared to R using steps that are small compared to R . Different map sizes and steps are chosen depending on the dislocation density. We note that very close numbers, 4 to 6 dislocations providing screening of the dislocation strain fields, are obtained for plastically deformed metals [38] by an XRD line profile analysis method that is close to our approach for GaN films.

The screening distances are obtained directly by calculating the correlation functions from the measured maps and do not require simulations. The same analysis can be carried out for more complicated dislocation distributions, when a simulation of the strain maps is not as straightforward as in our case. We have performed simulations of the maps to better understand them, but this is not necessary in every case where the screening distance is of interest.

4.3. Geometrically necessary dislocations

Maps of the strain and rotation components are commonly used in EBSD studies to determine the densities of geometrically necessary dislocations (GND) [39–44]. The GND density corresponds to the minimum density of dislocations that is required to provide a net effect that is of interest [45, 46]. It is therefore dependent on the scale of that effect and implies an appropriate spatial averaging of the strains and rotations at smaller scales. The papers cited above use the concept of GND to describe boundaries between misoriented domains or plastic bending of a crystal. The GND value is then a minimum density of dislocations that provides a small angle boundary or the curvature of the crystal lattice. In these cases, strain variations can be neglected compared to the lattice rotations, and the GND can be obtained from the differences in rotations between neighboring points in the measured maps.

Threading dislocations in GaN films are an example of a system where the concept of GND requires a different consideration. The screening distances R that we have found provide a scale for the determination of the GND. Counting dislocations on a smaller scale gives the density of statistically stored dislocations, while the strain averaged over distances exceeding R can be treated as due to the GND. The GND density for threading dislocations in GaN films is zero, since the dislocations screen each other's strain fields and do not provide a net long-range effect. More specifically, the strains and rotations are zero after averaging over the areas exceeding the screening distance R in the respective sample. To obtain this zero average, the step size of a measurement has to be small compared to R . In the studies cited above, the GND density is obtained from the differences in rotations between neighboring points without an average over

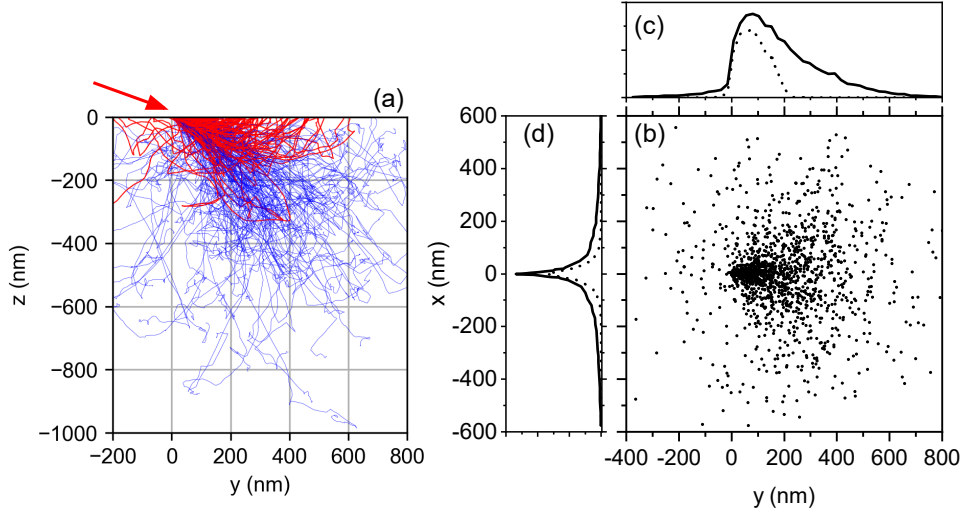


Figure 7: (a) Side view of the electron trajectories in GaN simulated by CASINO, (b) top view of the exit points of the trajectories of backscattered electrons and (c,d) distributions of the exit points in projections on the x and y axes. Dashed lines are the distributions of the exit points of the electrons that lost less than 10% of the initial energy. The incident electron beam (shown by a red arrow) of energy 15 keV is inclined by 70° along the y axis.

the points that would be measured in between. In our samples, strain and rotation maps measured with a step larger than R would only show an uncorrelated random distribution with the same probability density as our strain maps. The difference between neighboring measured points would not contain any feasible information if the step of the measurements is chosen larger than R . On the other end, a measurement with a step small compared to R would provide a local dislocation density that is needed to generate the particular strain and rotation maps. This latter treatment of GND is applied in Ref. [16] to a very similar case of threading dislocations in (In,Al)N films.

4.4. Spatial resolution of EBSD maps

We find that the correlation functions deviate from the $\propto \ln r$ law at small distances and become more gradual. Also, the EBSD maps of sample 2 with high dislocation density measured with a step between the measuring points of only 20 nm, show a clear distinction between the x and y directions. A comparison of the correlations in the x and y directions and Monte Carlo simulations allow us to estimate the spatial resolution of the EBSD maps to be $20 \times 200 \text{ nm}^2$, with the worse resolution along the direction of the tilt of the incident electron beam. In metals, grain boundaries are used for a direct measurement of the resolution, which depends on the material and the accelerating voltage (we refer to the papers [47, 48] which also provide literature reviews). The resolutions in x and y directions are obtained by appropriately orienting the grain boundary with respect to the direction of the electron beam. The resolution that we obtain is comparable to that obtained in relatively light metals but shows a larger anisotropy between the x and y directions.

For additional insight, we simulate the trajectories of the electrons in GaN using the free software CASINO [49]. Figure 7(a) is a side view on the electron trajectories. Red lines are trajectories of the backscattered electrons. A top view of their exit points is shown in Fig. 7(b). Their spatial distribution is

very asymmetric with respect to the x and y directions. The projections of the outcrop distributions on the x and y axes in Figs. 7(c,d) are even broader than the resolution that we obtain from the simulations of the strain and rotation maps. Since low-loss electrons provide the major contribution to EBSD patterns [50], we plot by dotted lines in Figs. 7(c,d) the distributions of electrons that lost less than 10% of their initial energy of 15 keV. The widths of these distributions are consistent with the resolution that we found.

The EBSD maps of the dislocation-free GaN sample 0 show only uncorrelated random noise for all strain and rotation components. The widths of these distributions are an order of magnitude larger compared to Si(001). We also note that the XRD curves of this sample, albeit narrow compared to the other samples, are significantly broader than expected for its dislocation density [19]. The EBSD measurements on GaN sample 0 were performed before and after surface cleaning, which had a negligible effect on the strain distributions. Hence, neither surface roughness nor contamination do appear to be responsible for the apparent strain in this sample.

In the absence of dislocations, the remaining source of strain are point defects, including impurities as well as native defects. The density of native defects in GaN is orders of magnitude larger than in Si. The density of Ga vacancies alone in GaN ranges from 10^{16} – 10^{18} cm^{-3} [51–53], as compared to a vacancy density below $1 \times 10^{14} \text{ cm}^{-3}$ in Si [54, 55]. To examine the effect of point defects, we have performed simulations of their strain maps, assuming a spatially random distribution of dilatation centers with the excess volume equal to the atomic volume. Even for a density of 10^{18} cm^{-3} , the strain produced by these centers is too low to account for the experimentally measured strain in Fig. 3(a). Moreover, the simulated strain maps exhibit the same anisotropy as seen in Fig. 3(c) caused by the inclination of the incident electron beam.

The distributions of the shear strains ε_{13} and ε_{23} coincide

in all three GaN samples and are therefore independent of the dislocation density. These strains have to be zero due to the stress free boundary conditions. Of the three zero stress conditions at the surface $\sigma_{i3} = 0$ ($i = 1, 2, 3$), one condition, $\sigma_{33} = 0$, is used in the processing of the Kikuchi patterns. The other two conditions reduce to $\varepsilon_{13} = 0$ and $\varepsilon_{23} = 0$ for the (0001) surface of a hexagonal crystal. The distributions of these components thus provide an estimate of the sensitivity limit to dislocation strains. We note that the maps of these components do not show any correlations in the crystals with dislocations, in contrast to other strain and rotation components that develop correlations. Thus, in the case where a dislocation free crystal is not available as a reference, the distributions of these shear strain components can provide an estimate of the accuracy of the other strain and rotation maps.

5. Summary

The screening of the dislocation strains by the surrounding dislocations is revealed by both fits of the XRD curves in reciprocal space and the real space correlations in the EBSD strain maps. It is shown that the characteristic screening distance can be derived with a higher accuracy from the EBSD strain and rotation maps than from XRD profiles. Screening distances of 2 μm and 0.3 μm are obtained for the GaN films with threading dislocation densities of $5 \times 10^8 \text{ cm}^{-2}$ and $1.8 \times 10^{10} \text{ cm}^{-2}$, respectively, which indicates that the dislocation strain is screened by only 4 neighboring dislocations in both samples. The strain maps from the high dislocation density sample measured with a small step size show a large anisotropy in the resolution of the EBSD measurements. The resolution is estimated to be $20 \times 200 \text{ nm}^2$, with the worse resolution in the direction corresponding to the inclination of the incident electron beam. XRD curves and EBSD maps are simulated by the Monte Carlo method within one and the same model of dislocation distributions. We find that XRD overestimates the dislocation densities, presumably due to contributions from the strained region near the film–substrate interface. In contrast, EBSD measurements on a sample with a high dislocation density underestimate the strain, presumably due to large strain gradients within the probed volume.

Acknowledgments

The authors thank Bernd Jenichen for XRD measurements on sample 2 made for our former study [19], Jingxuan Kang for cleaning sample 0 and Moritz Hansemann for AFM measurements of that sample, as well as Achim Trampert for a critical reading of the manuscript.

References

- [1] D. Hull, D. J. Bacon, *Introduction to Dislocations*, Elsevier, Amsterdam, 2011, Ch. 4.4. doi:10.1016/C2009-0-64358-0. URL <https://doi.org/10.1016/C2009-0-64358-0>
- [2] M. Wilkens, Das mittlere Spannungsquadrat $\langle \sigma^2 \rangle$ begrenzt regellos verteilter Versetzungen in einem zylinderförmigen Körper, *Acta Metall.* 17 (1969) 1155–1159. doi:10.1016/0001-6160(69)90092-3. URL <https://www.sciencedirect.com/science/article/abs/pii/0001616069900923>
- [3] M. Wilkens, Theoretical aspects of kinematical x-ray diffraction profiles from crystals containing dislocation distributions, in: J. A. Simmons, R. de Wit, R. Bullough (Eds.), *Fundamental Aspects of Dislocation Theory*, Nat. Bur. Stand. (U.S.) Spec. Publ., Washington, D.C., 1970, pp. 1195–1221. 1
- [4] G. Ribárik, T. Ungár, J. Gubicza, *MWP-fit: a program for multiple whole-profile fitting of diffraction peak profiles by ab initio theoretical functions*, *J. Appl. Cryst.* 34 (2001) 669–676. doi:10.1107/S0021889801011451. URL <https://scripts.iucr.org/cgi-bin/paper?S0021889801011451>
- [5] P. Scardi, M. Leoni, *Whole powder pattern modelling*, *Acta Cryst. A* 58 (2002) 190–200. doi:10.1107/S0108767301021298. URL <https://scripts.iucr.org/cgi-bin/paper?S0108767301021298>
- [6] V. M. Kaganer, K. K. Sabelfeld, *Strain distributions and diffraction peak profiles from crystals with dislocations*, *Acta Cryst. A* 70 (2014) 457–471. doi:10.1107/S2053273314011139. URL <https://scripts.iucr.org/cgi-bin/paper?S2053273314011139>
- [7] V. M. Kaganer, K. K. Sabelfeld, *X-ray diffraction peaks from correlated dislocations: Monte Carlo study of dislocation screening*, *Acta Cryst. A* 66 (2010) 703–716. doi:10.1107/S0108767310033544. URL <https://scripts.iucr.org/cgi-bin/paper?S0108767310033544>
- [8] A. Borbély, A. Aoufi, D. Becht, *X-ray methods for strain energy evaluation of dislocated crystals*, *J. Appl. Cryst.* 56 (2023) 254–262. doi:10.1107/S1600576722012262. URL <https://scripts.iucr.org/cgi-bin/paper?S1600576722012262>
- [9] C. Richter, V. M. Kaganer, A. Even, A. Dussaigne, P. Ferret, F. Barbier, Y.-M. Le Vaillant, T. U. Schüllli, *Nanoscale mapping of the full strain tensor, rotation, and composition in partially relaxed $\text{In}_x\text{Ga}_{1-x}\text{N}$ layers by scanning X-ray diffraction microscopy*, *Phys. Rev. Applied* 18 (2022) 064015. doi:10.1103/PhysRevApplied.18.064015. URL <https://link.aps.org/doi/10.1103/PhysRevApplied.18.064015>
- [10] J. A. Venables, C. J. Harland, *Electron back-scattering patterns—A new technique for obtaining crystallographic information in the scanning electron microscope*, *Philos. Magazine* 27 (1973) 1193–1200. doi:10.1080/14786437308225827. URL <http://www.tandfonline.com/doi/abs/10.1080/14786437308225827>
- [11] A. J. Schwartz, M. Kumar, B. L. Adams, D. P. Field (Eds.), *Electron Backscatter Diffraction in Materials Science*, Springer, Boston, 2009. doi:10.1007/978-0-387-88136-2. URL <https://link.springer.com/10.1007/978-0-387-88136-2>
- [12] A. J. Wilkinson, T. B. Britton, *Strains, planes, and EBSD in materials science*, *Materials Today* 15 (2012) 366–376. doi:10.1016/S1369-7021(12)70163-3. URL <https://linkinghub.elsevier.com/retrieve/pii/S1369702112701633>
- [13] A. J. Wilkinson, G. Meaden, D. J. Dingley, *High resolution mapping of strains and rotations using electron backscatter diffraction*, *Mater. Sci. Technol.* 22 (2006) 1271–1278. doi:10.1179/174328406X130966. URL <http://www.tandfonline.com/doi/full/10.1179/174328406X130966>
- [14] A. J. Wilkinson, G. Meaden, D. J. Dingley, *High-resolution elastic strain measurement from electron backscatter diffraction patterns: New levels of sensitivity*, *Ultramicroscopy* 106 (2006) 307–313. doi:10.1016/j.ultramic.2005.10.001. URL <https://linkinghub.elsevier.com/retrieve/pii/S0304399105002251>
- [15] A. J. Wilkinson, E. Tarleton, A. Vilalta-Clemente, J. Jiang, T. B. Britton, D. M. Collins, *Measurement of probability distributions for internal stresses in dislocated crystals*, *Appl. Phys. Lett.* 105 (2014) 181907.

- doi:10.1063/1.4901219.
URL <http://aip.scitation.org/doi/10.1063/1.4901219> 1, 4.1
- [16] A. Vilalta-Clemente, G. Naresh-Kumar, M. Nouf-Allahiani, P. Gamarra, M. di Forte-Poisson, C. Trager-Cowan, A. Wilkinson, **Cross-correlation based high resolution electron backscatter diffraction and electron channelling contrast imaging for strain mapping and dislocation distributions in InAlN thin films**, *Acta Mater.* 125 (2017) 125–135. doi:10.1016/j.actamat.2016.11.039.
URL <https://linkinghub.elsevier.com/retrieve/pii/S1359645416309065> 3.2, 4.3
- [17] S. Kalácska, I. Groma, A. Borbély, P. D. Ispánovity, **Comparison of the dislocation density obtained by HR-EBSD and X-ray profile analysis**, *Appl. Phys. Lett.* 110 (2017) 091912. doi:10.1063/1.4977569.
URL <https://pubs.aip.org/apl/article/110/9/091912/34380/Comparison-of-the-dislocation-density-obtained-by> 1
- [18] J. Gallet, M. Perez, R. Guillou, C. Ernould, C. Le Bourlot, C. Langlois, B. Beausir, E. Bouzy, T. Chaise, S. Cazottes, **Experimental measurement of dislocation density in metallic materials: A quantitative comparison between measurements techniques (XRD, R-ECCL, HR-EBSD, TEM)**, *Mater. Characterization* 199 (2023) 112842. doi:10.1016/j.matchar.2023.112842.
URL <https://linkinghub.elsevier.com/retrieve/pii/S1044580323002000> 1
- [19] V. M. Kaganer, B. Jenichen, M. Ramsteiner, U. Jahn, C. Hauswald, F. Grosse, S. Fernández-Garrido, O. Brandt, **Quantitative evaluation of the broadening of x-ray diffraction, Raman, and photoluminescence lines by dislocation-induced strain in heteroepitaxial GaN films**, *J. Phys. D: Appl. Phys.* 48 (2015) 385105. doi:10.1088/0022-3727/48/38/385105.
URL <https://iopscience.iop.org/article/10.1088/0022-3727/48/38/385105> 2.1, 2.4, 4.4, 5
- [20] O. Brandt, V. M. Kaganer, J. Lähmemann, T. Flissikowski, C. Pfüller, K. K. Sabelfeld, A. E. Kireeva, C. Chèze, R. Calarco, H. T. Grahn, U. Jahn, **Carrier diffusion in GaN: A cathodoluminescence study. II. Ambipolar versus exciton diffusion**, *Phys. Rev. Applied* 17 (2022) 024018. doi:10.1103/PhysRevApplied.17.024018.
URL <https://link.aps.org/doi/10.1103/PhysRevApplied.17.024018> 2.1
- [21] J. Lähmemann, V. M. Kaganer, K. K. Sabelfeld, A. E. Kireeva, U. Jahn, C. Chèze, R. Calarco, O. Brandt, **Carrier diffusion in GaN: A cathodoluminescence study. III. Nature of nonradiative recombination at threading dislocations**, *Phys. Rev. Applied* 17 (2022) 024019. doi:10.1103/PhysRevApplied.17.024019.
URL <https://link.aps.org/doi/10.1103/PhysRevApplied.17.024019> 2.1
- [22] S. J. Rosner, E. C. Carr, M. J. Ludowise, G. Girolami, H. I. Erikson, **Correlation of cathodoluminescence inhomogeneity with microstructural defects in epitaxial GaN grown by metalorganic chemical-vapor deposition**, *Appl. Phys. Lett.* 70 (1997) 420. doi:10.1063/1.118322.
URL <https://pubs.aip.org/apl/article/70/4/420/520280/Correlation-of-cathodoluminescence-inhomogeneity> 2.1
- [23] T. Sugahara, H. Sato, M. Hao, Y. Naoi, S. Kurai, S. T. K. Yamashita, K. Nishino, L. T. Romano, S. Sakai, **Direct evidence that dislocations are non-radiative recombination centers in GaN**, *Jpn. J. Appl. Phys.* 37 (1998) L398. doi:10.1143/JJAP.37.L398.
URL <https://iopscience.iop.org/article/10.1143/JJAP.37.L398>
- [24] J. S. Speck, S. J. Rosner, **The role of threading dislocations in the physical properties of GaN and its alloys**, *Physica B* 273 (1999) 24–32. doi:10.1016/S0921-4526(99)00399-3.
URL <https://www.sciencedirect.com/science/article/abs/pii/S0921452699003993>
- [25] N. Pauc, M. R. Phillips, V. Aimez, D. Drouin, **Carrier recombination near threading dislocations in GaN epilayers by low voltage cathodoluminescence**, *Appl. Phys. Lett.* 89 (2006) 161905. doi:10.1063/1.2357881.
URL <https://pubs.aip.org/apl/article/89/16/161905/128695/Carrier-recombination-near-threading-dislocations>
- [26] V. M. Kaganer, K. K. Sabelfeld, O. Brandt, **Piezoelectric field, exciton lifetime, and cathodoluminescence intensity at threading dislocations in GaN(0001)**, *Appl. Phys. Lett.* 112 (2018) 122101. doi:10.1063/1.5022170.
URL <http://aip.scitation.org/doi/10.1063/1.5022170> 2.1
- [27] M. Khoury, A. Courville, B. Poulet, M. Teisseire, E. Beraudo, M. J. Rashid, E. Frayssinet, B. Damilano, F. Semond, O. Tottereau, P. Venéguès, **Imaging and counting threading dislocations in c-oriented epitaxial GaN layers**, *Semicond. Sci. Technol.* 28 (2013) 035006. doi:10.1088/0268-1242/28/3/035006.
URL <https://iopscience.iop.org/article/10.1088/0268-1242/28/3/035006> 2.1
- [28] V. Srikant, J. S. Speck, D. R. Clarke, **Mosaic structure in epitaxial thin films having large lattice mismatch**, *J. Appl. Phys.* 82 (1997) 4286. doi:10.1063/1.366235.
URL <https://pubs.aip.org/jap/article/82/9/4286/492583/Mosaic-structure-in-epitaxial-thin-films-having> 2.2
- [29] Y. J. Sun, O. Brandt, T. Y. Liu, A. Trampert, K. H. Ploog, **Determination of the azimuthal orientational spread of GaN films by x-ray diffraction**, *Appl. Phys. Lett.* 81 (2002) 4928. doi:10.1063/1.1531832.
URL <https://pubs.aip.org/apl/article/81/26/4928/510708/Determination-of-the-azimuthal-orientational>
- [30] V. M. Kaganer, O. Brandt, A. Trampert, K. H. Ploog, **X-ray diffraction peak profiles from threading dislocations in GaN epitaxial films**, *Phys. Rev. B* 72 (2005) 045423. doi:10.1103/PhysRevB.72.045423.
URL <https://link.aps.org/doi/10.1103/PhysRevB.72.045423> 2.2, 2.4, 2, 3.1, 4.1, 4.2
- [31] E. D. Wolf, M. Braunstein, A. I. Braunstein, **Pseudo-Kikuchi pattern decoration by a thin amorphous silicon film**, *Applied Physics Letters* 15 (1969) 389–391. doi:10.1063/1.1652871.
URL <https://pubs.aip.org/apl/article/15/12/389/41688/PSEUDO-KIKUCHI-PATTERN-DEGRADATION-BY-A-THIN> 1
- [32] A. J. Wilkinson, G. Meaden, D. J. Dingley, **Mapping strains at the nanoscale using electron back scatter diffraction**, *Superlattices and Microstructures* 45 (2009) 285–294. doi:10.1016/j.spmi.2008.10.046.
URL <https://linkinghub.elsevier.com/retrieve/pii/S0749603608002462> 2.3
- [33] A. Polian, M. Grimsditch, I. Grzegory, **Elastic constants of gallium nitride**, *J. Appl. Phys.* 79 (1996) 3343–3344. doi:10.1063/1.361236.
URL <https://pubs.aip.org/jap/article/79/6/3343/2080/Elastic-constants-of-gallium-nitride> 2.3, 2.4
- [34] V. M. Kaganer, **X-ray diffraction from dislocation half-loops in epitaxial films**, *J. Appl. Cryst.* 57 (2024) 276–283. doi:10.1107/S160057672400089X.
URL <https://scripts.iucr.org/cgi-bin/paper?S160057672400089X> 2.4
- [35] A. Y. Belov, in: V. L. Indenbom, J. Lothe (Eds.), *Elastic Strain Fields and Dislocation Mobility*, North-Holland, Amsterdam, 1992, Ch. 6. doi:DOI:10.1016/B978-0-444-88773-3.50013-3, [link].
URL <https://linkinghub.elsevier.com/retrieve/pii/B9780444887733500133> 2.4
- [36] J. Lothe, in: V. L. Indenbom, J. Lothe (Eds.), *Elastic Strain Fields and Dislocation Mobility*, North-Holland, Amsterdam, 1992, Ch. 5. doi:10.1016/B978-0-444-88773-3.50012-1, [link].
URL <https://linkinghub.elsevier.com/retrieve/pii/B9780444887733500121> 2.4
- [37] V. S. Kopp, V. M. Kaganer, M. V. Baidakova, W. V. Lundin, A. E. Nikolaev, E. V. Verkhovtceva, M. A. Yagovkina, N. Cherkashin, **X-ray determination of threading dislocation densities in GaN/Al₂O₃(0001) films grown by metalorganic vapor phase epitaxy**, *J. Appl. Phys.* 115 (2014) 073507. doi:10.1063/1.4865502.
URL <http://aip.scitation.org/doi/10.1063/1.4865502> 4.1
- [38] A. Borbély, J. Driver, T. Ungár, **An X-ray method for the determination of stored energies in texture components of deformed metals; application to cold worked ultra high purity iron**, *Acta Mater.* 48 (2000) 2005–2016. doi:10.1016/s1359-6454(99)00457-7.
URL <https://linkinghub.elsevier.com/retrieve/pii/S1359645499004577> 4.2
- [39] S. Sun, B. L. Adams, W. E. King, **Observations of lattice curvature near the interface of a deformed aluminium bicrystal**, *Philos. Mag.* A 80 (2000) 9–25. doi:10.1080/01418610008212038.
URL <http://www.tandfonline.com/doi/abs/10.1080/01418610008212038> 4.3

- [40] B. El-Dasher, B. Adams, A. Rollett, Viewpoint: experimental recovery of geometrically necessary dislocation density in polycrystals, *Scripta Mater.* 48 (2003) 141–145. doi:10.1016/S1359-6462(02)00340-8. URL <https://linkinghub.elsevier.com/retrieve/pii/S1359646202003408>
- [41] W. Pantleon, Resolving the geometrically necessary dislocation content by conventional electron backscattering diffraction, *Scripta Mater.* 58 (11) (2008) 994–997. doi:10.1016/j.scriptamat.2008.01.050. URL <https://linkinghub.elsevier.com/retrieve/pii/S1359646208000912>
- [42] B. L. Adams, J. Kacher, EBSD-based microscopy: resolution of dislocation density, *CMC* 14 (2009) 185–196. doi:10.3970/cmc.2009.014.185. URL <https://www.techscience.com/cmc/v14n3/22513>
- [43] A. J. Wilkinson, D. Randman, Determination of elastic strain fields and geometrically necessary dislocation distributions near nanoindentations using electron back scatter diffraction, *Philos. Mag.* 90 (9) (2010) 1159–1177. doi:10.1080/14786430903304145. URL <http://www.tandfonline.com/doi/abs/10.1080/14786430903304145>
- [44] J. Jiang, T. Britton, A. Wilkinson, Measurement of geometrically necessary dislocation density with high resolution electron backscatter diffraction: Effects of detector binning and step size, *Ultramicroscopy* 125 (2013) 1–9. doi:10.1016/j.ultramic.2012.11.003. URL <https://linkinghub.elsevier.com/retrieve/pii/S0304399112002823>
- [45] F. Nye, Some geometrical relations in dislocated crystals, *Acta Metallurg.* 1 (1953) 153–162. doi:10.1016/0001-6160(53)90054-6. URL <https://www.sciencedirect.com/science/article/pii/0001616053900546>
- [46] A. Arsenlis, D. Parks, Crystallographic aspects of geometrically-necessary and statistically-stored dislocation density, *Acta Mater.* 47 (1999) 1597–1611. doi:10.1016/S1359-6454(99)00020-8. URL <https://linkinghub.elsevier.com/retrieve/pii/S1359645499000208>
- [47] D. R. Steinmetz, S. Zaefferer, Towards ultrahigh resolution EBSD by low accelerating voltage, *Materials Sci. Technol.* 26 (2010) 640–645. doi:10.1179/026708309X12506933873828. URL <https://journals.sagepub.com/doi/full/10.1179/026708309X12506933873828>
- [48] A. Tripathi, S. Zaefferer, On the resolution of EBSD across atomic density and accelerating voltage with a particular focus on the light metal magnesium, *Ultramicroscopy* 207 (2019) 112828. doi:10.1016/j.ultramic.2019.112828. URL <https://linkinghub.elsevier.com/retrieve/pii/S0304399119301901>
- [49] D. Drouin, A. R. Couture, D. Joly, X. Tastet, V. Aimez, R. Gauvin, CASINO V2.42 — A fast and easy-to-use modeling tool for scanning electron microscopy and microanalysis users, *Scanning* 29 (2007) 92–101. doi:10.1002/sca.20000. URL <https://onlinelibrary.wiley.com/doi/10.1002/sca.20000>
- [50] A. Deal, T. Hooghan, A. Eades, Energy-filtered electron backscatter diffraction, *Ultramicroscopy* 108 (2008) 116–125. doi:10.1016/j.ultramic.2007.03.010. URL <https://linkinghub.elsevier.com/retrieve/pii/S0304399107000836>
- [51] K. Saarinen, T. Laine, S. Kuisma, J. Nissilä, P. Hautojärvi, L. Dobrzynski, J. M. Baranowski, K. Pakula, R. Stepniewski, M. Wojdak, A. Wyszomolek, T. Suski, M. Leszczynski, I. Grzegory, S. Porowski, Observation of Native Ga Vacancies in GaN by Positron Annihilation, *Physical Review Letters* 79 (1997). 4.4
- [52] K. Saarinen, P. Seppälä, J. Oila, P. Hautojärvi, C. Corbel, O. Briot, R. L. Aulombard, Gallium vacancies and the growth stoichiometry of GaN studied by positron annihilation spectroscopy, *Applied Physics Letters* 73 (1998) 3253–3255. doi:10.1063/1.122735. URL <https://pubs.aip.org/apl/article/73/22/3253/69218/Gallium-vacancies-and-the-growth-stoichiometry-of>
- [53] J. Oila, J. Kivioja, V. Ranki, K. Saarinen, D. C. Look, R. J. Molnar, S. S. Park, S. K. Lee, J. Y. Han, Ga vacancies as dominant intrinsic acceptors in GaN grown by hydride vapor phase epitaxy, *Applied Physics Letters* 82 (2003) 3433–3435. doi:10.1063/1.1569414. URL <https://pubs.aip.org/apl/article/82/20/3433/513530/Ga-vacancies-as-dominant-intrinsic-acceptors-in>
- [54] V. V. Voronkov, R. Falster, Vacancy and self-interstitial concentration incorporated into growing silicon crystals, *Journal of Applied Physics* 86 (1999) 5975–5982. doi:10.1063/1.371642. URL <https://pubs.aip.org/jap/article/86/11/5975/514526/Vacancy-and-self-interstitial-concentration>
- [55] H. Bettin, K. Fujii, A. Nicolaus, Silicon spheres for the future realization of the kilogram and the mole, *Comptes Rendus. Physique* 20 (2019) 64–76. doi:10.1016/j.crhy.2018.12.005. URL <https://comptes-rendus.academie-sciences.fr/physique/articles/10.1016/j.crhy.2018.12.005/>

Supplementary Information

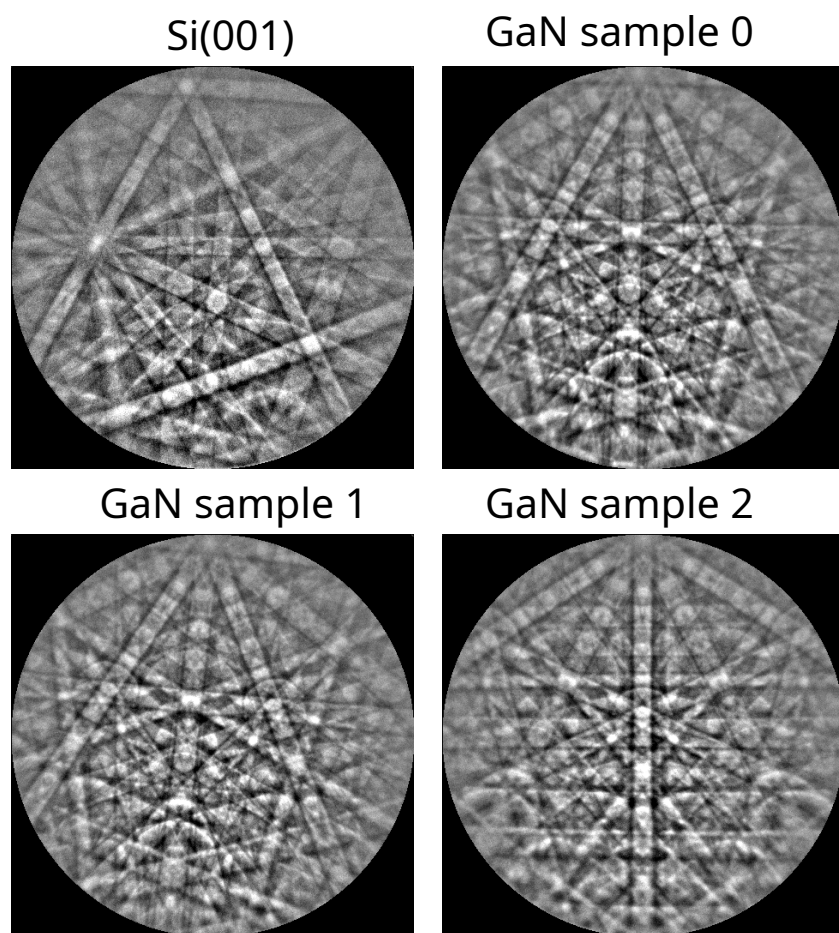


Figure S1: Kikuchi patterns of the GaN samples 0, 1, 2 and the Si wafer.

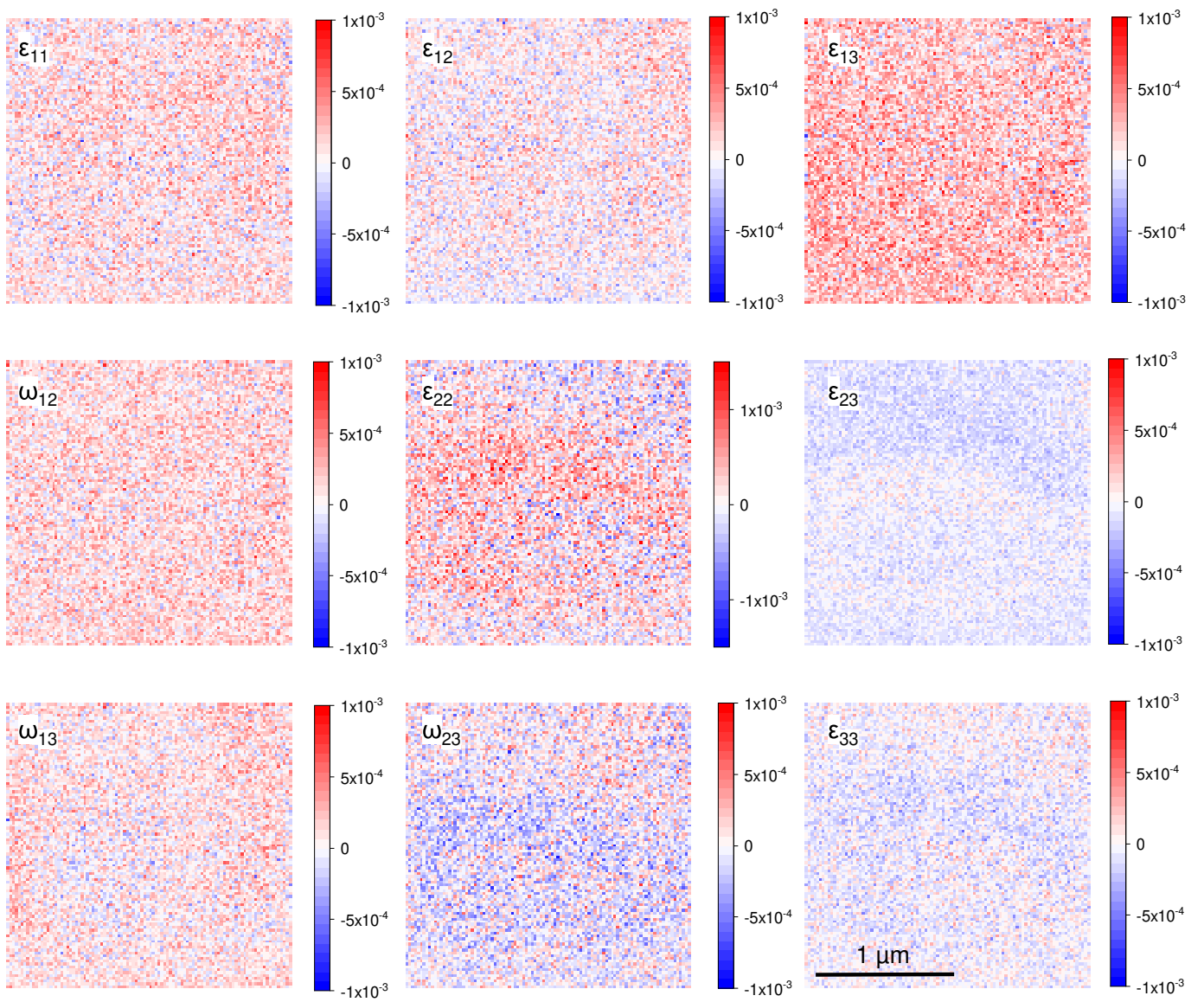


Figure S2: Components of the strain and rotation tensors of sample 0 (dislocation free GaN sample).

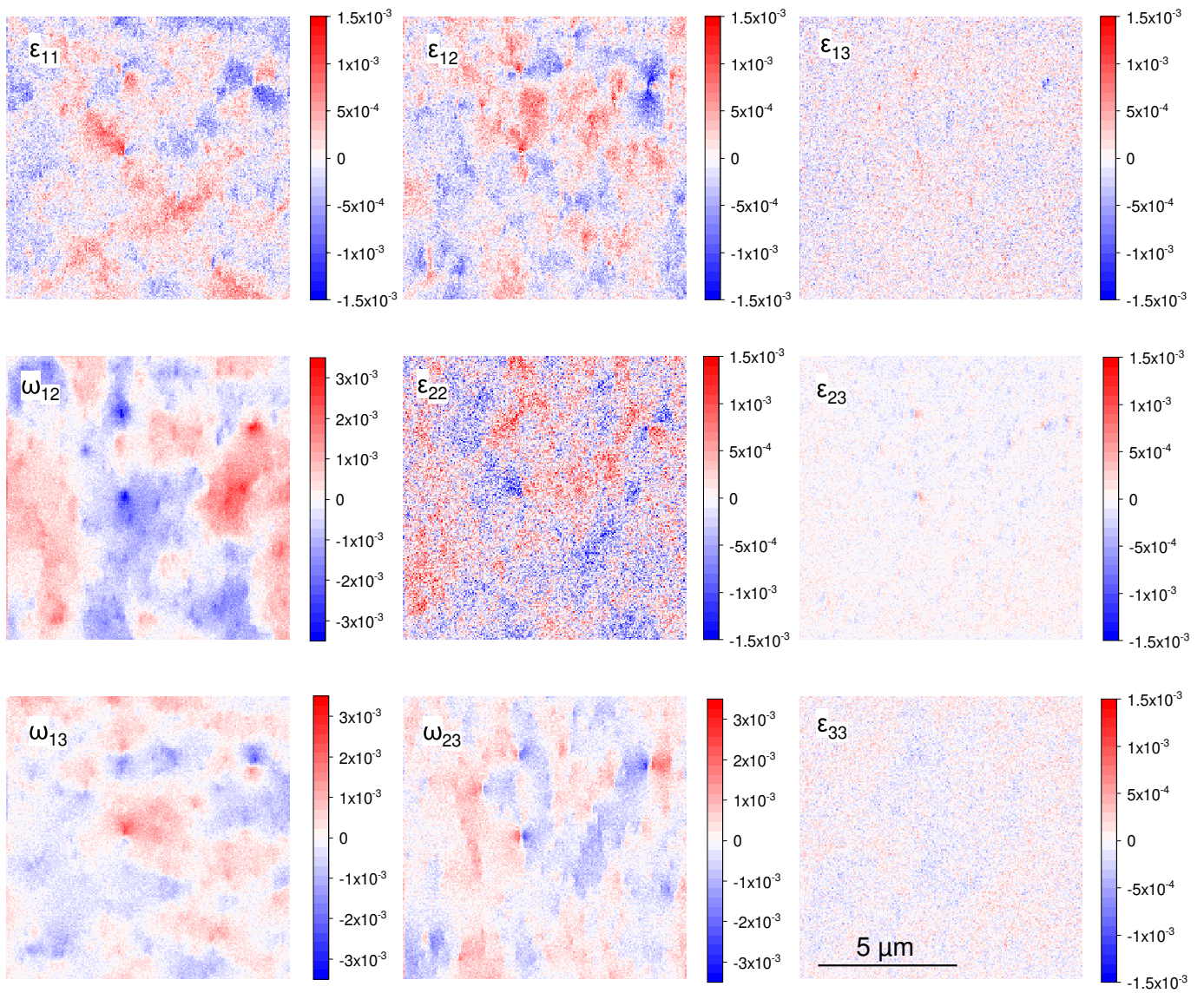


Figure S3: Components of the strain and rotation tensors of sample 1.

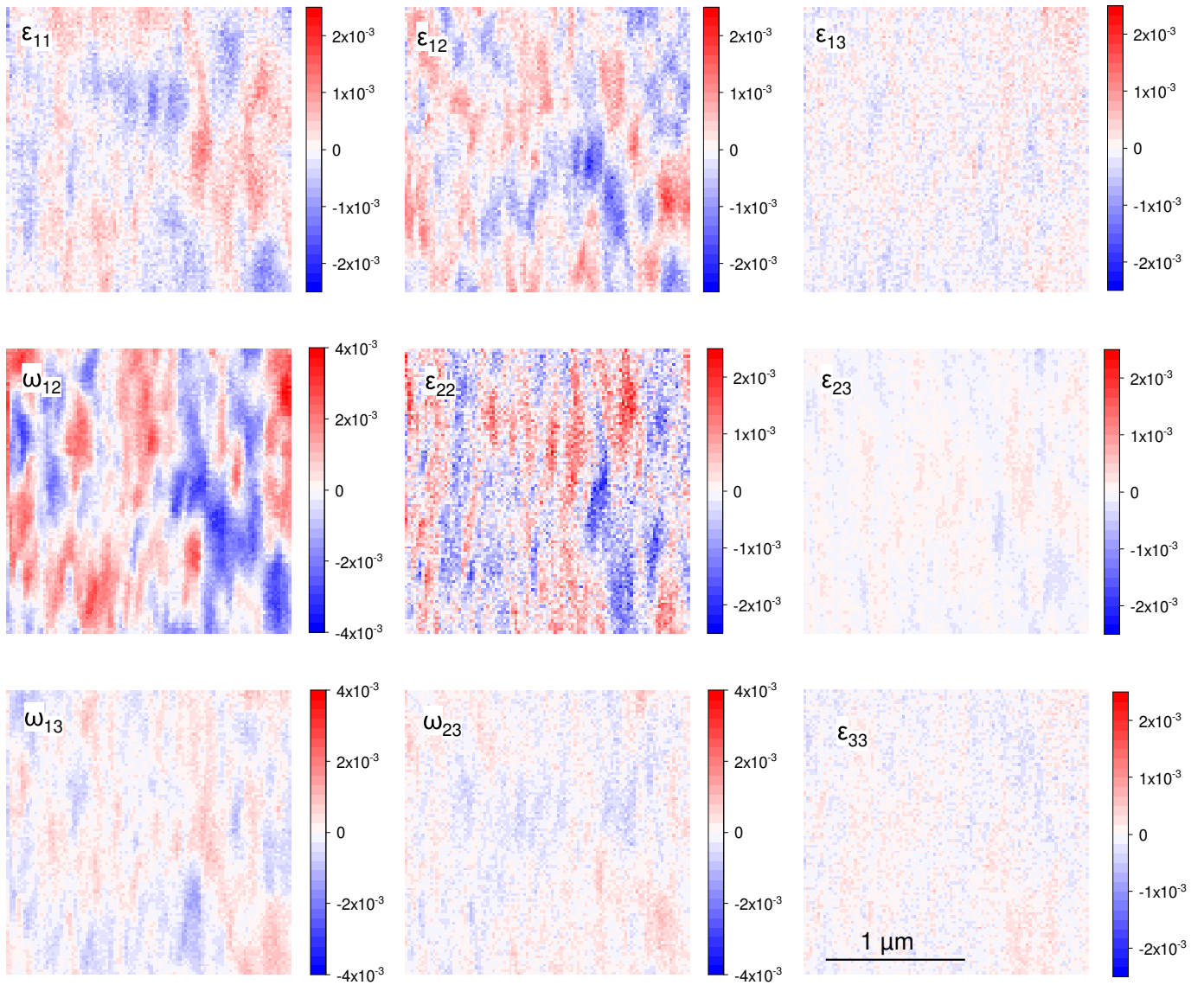


Figure S4: Components of the strain and rotation tensors of sample 2.

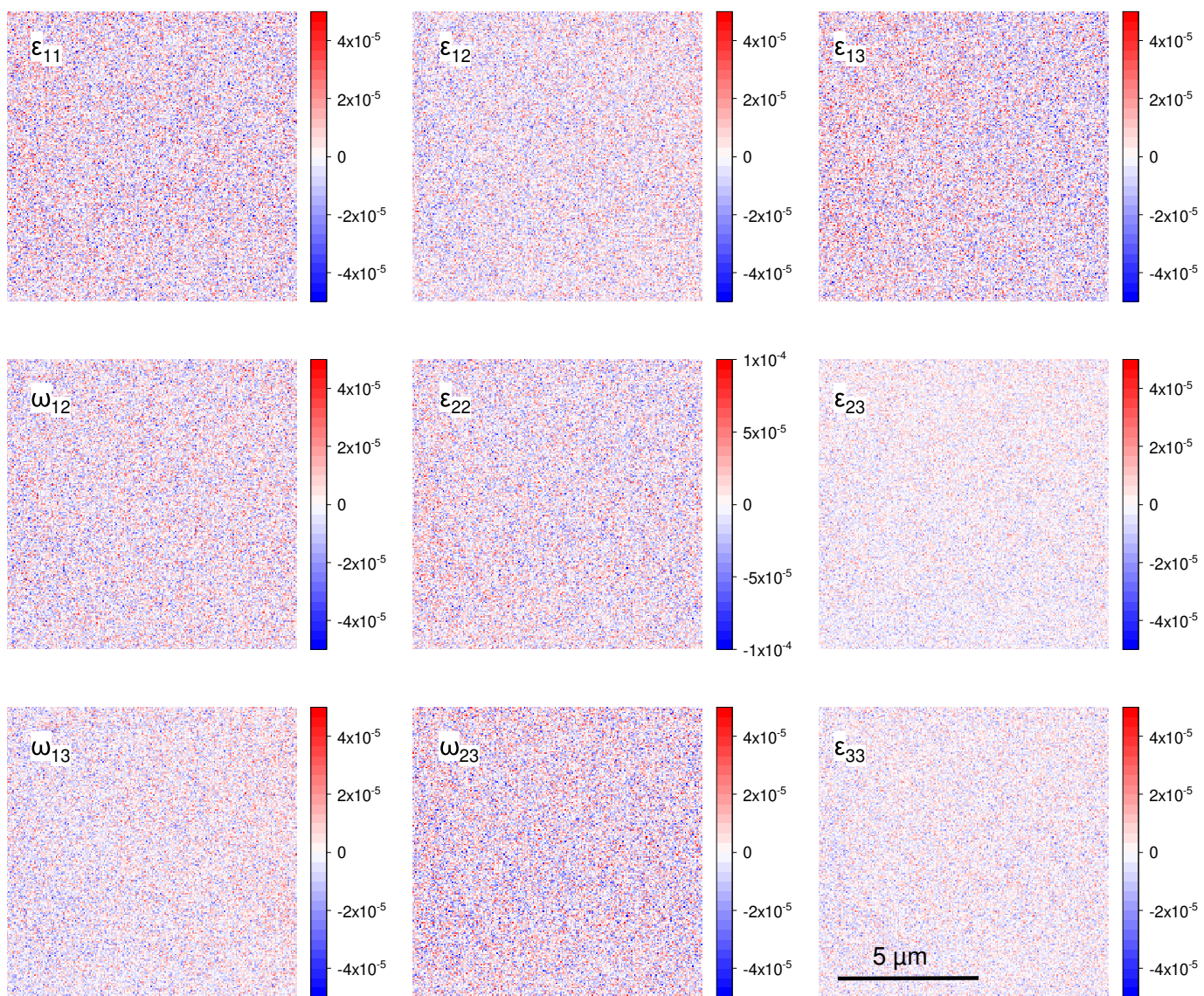


Figure S5: Components of the strain and rotation tensors of a silicon wafer. Note different ranges of the values in comparison to Fig. S2.

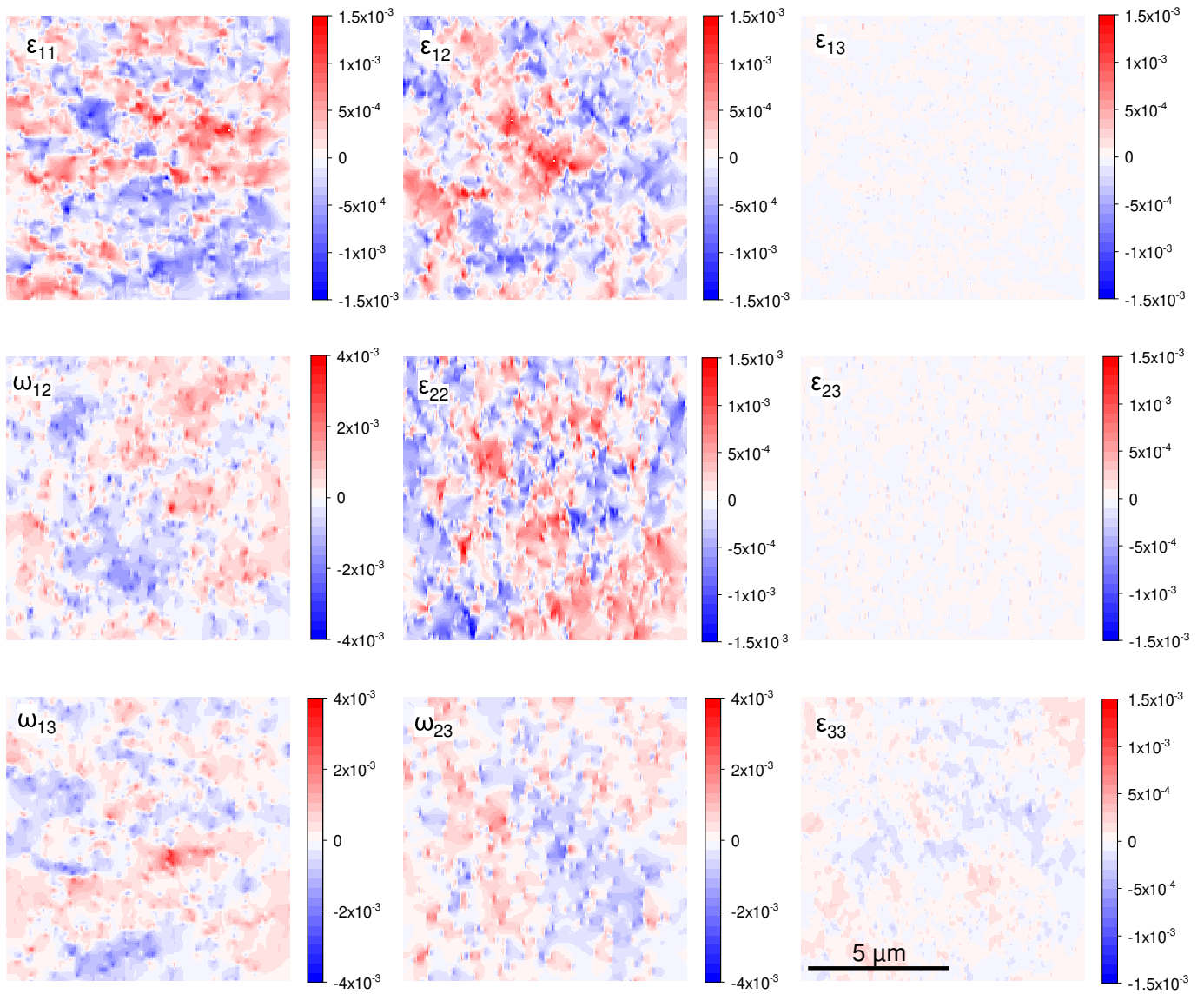


Figure S6: Monte Carlo simulation of the strain and rotation tensors of sample 1.

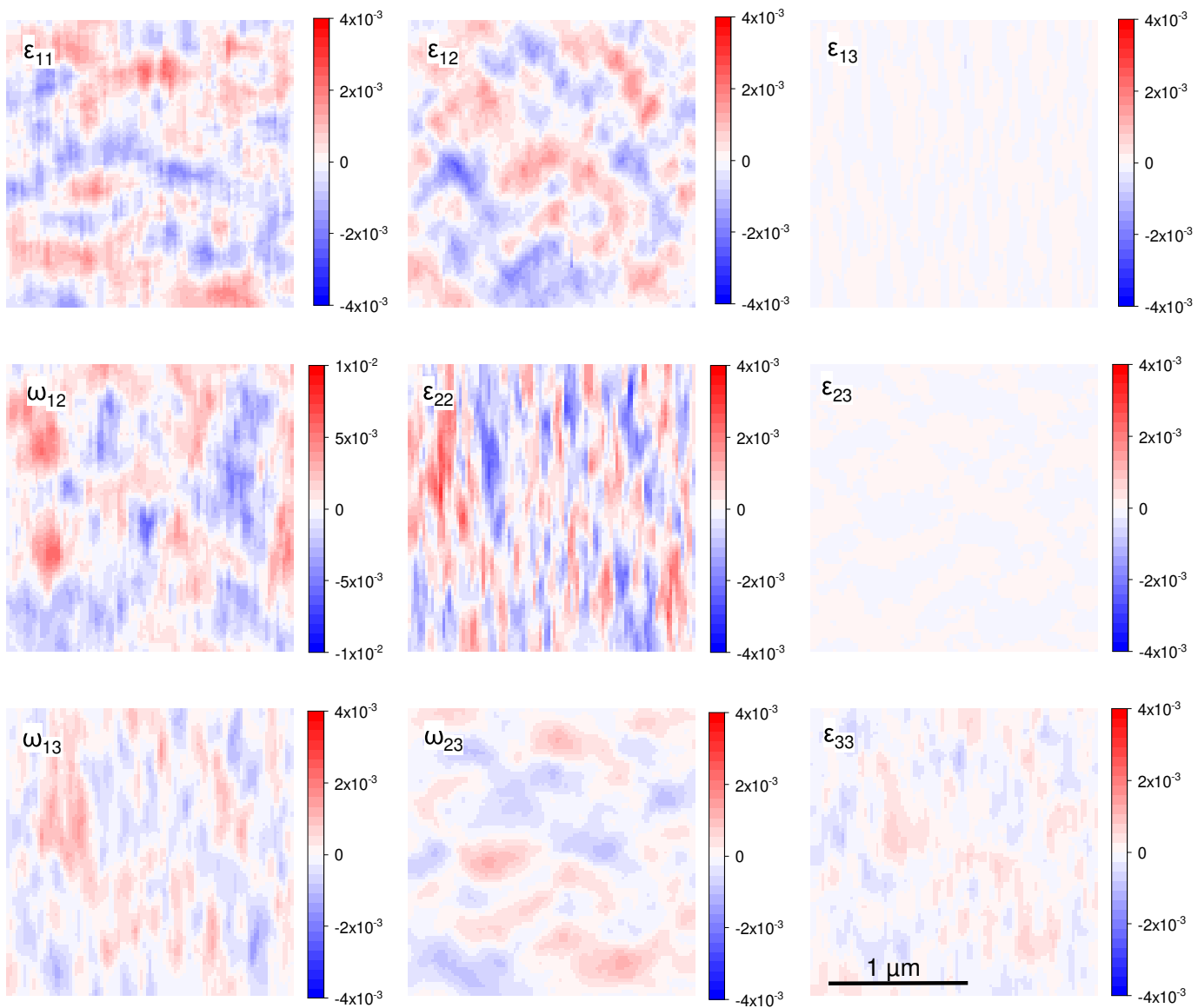


Figure S7: Monte Carlo simulation of the strain and rotation tensors of sample 2.

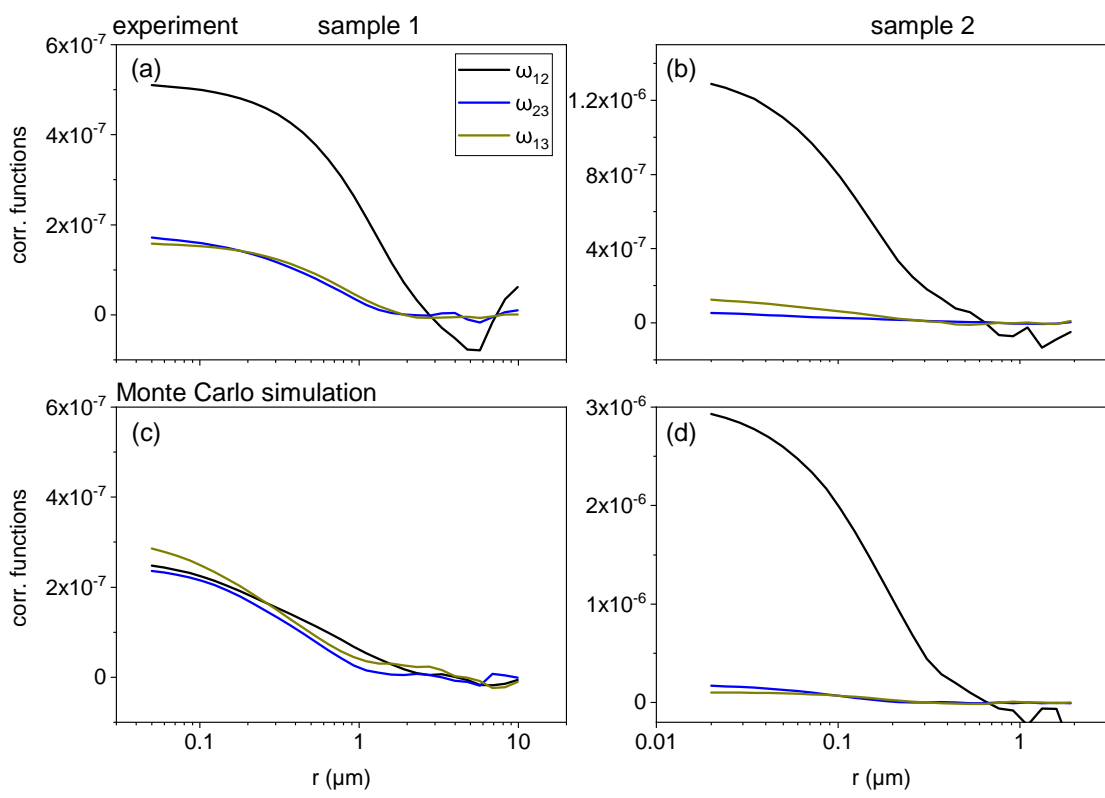


Figure S8: Orientation-averaged autocorrelation functions of the rotations (a,b) in the measured maps and (c,d) in Monte Carlo simulations.